Available online at www.sciencedirect.com

SciVerse ScienceDirect

Geochimica et Cosmochimica Acta 79 (2012) 79–105

Geochimica et Cosmochimica Acta

www.elsevier.com/locate/gca

# Amoeboid olivine aggregates (AOAs) in the Efremovka, Leoville and Vigarano (CV3) chondrites: A record of condensate evolution in the solar nebula

Alex Ruzicka [a,*], Christine Floss [b], Melinda Hutson [a]

[a] Cascadia Meteorite Laboratory, Portland State University, Department of Geology, 17 Cramer Hall, 1721 SW Broadway, Portland, OR 97207-0751, USA

[b] Laboratory for Space Sciences and Physics Department, Washington University, Campus Box 1105, St. Louis, MO 63130, USA

Received 29 November 2010; accepted in revised form 28 November 2011

**Abstract**

Amoeboid olivine aggregates (AOAs) in the Efremovka, Leoville, and Vigarano CV3 chondrites were studied using petrographic and microanalytical techniques to evaluate the origins of these inclusions and their relationships to other chondrite components. Our data support the idea that the inclusions formed by dust growth in the solar nebula as condensates and that they preserve a record of mineralogical and chemical evolution. Spinel-rich nodules and ribbons in AOAs often show Group II trace element patterns and formed either by fractional condensation or by condensation following partial vaporization. The dominant olivine component in AOAs can be explained as a condensate produced in the same way, but with fractionation occurring at a lower temperature. Other spinel-rich material in AOAs appears to be a vaporization residue. Ca-rich pyroxene + anorthite patches in AOAs show chemical signatures similar to those observed for spinel- or melilite-bearing regions but with lower refractory element and higher Mg and Si contents, supporting the idea that the patches formed by reaction between CAI-like material and Mg–Si-rich gas. Different trace element patterns (Group II and non-Group II refractory) are sometimes found for Al-rich regions (Ca-pyroxene + anorthite, or melilite-bearing) in a given AOA, suggesting that AOAs agglomerated from materials that formed under different conditions and that they did not subsequently homogenize. AOAs appear to have originated in a system with near-canonical solar composition and a low pressure gas ($\sim 10^{-6}$–$10^{-4}$ bar) over a range of temperatures (mainly ~1200–1384 K) under somewhat non-equilibrium conditions. Relative to predicted equilibrium condensates, most AOAs show an apparent paucity of metal, possibly reflecting differential, density-dependent sorting between olivine and metal grains during aggregate formation. Trace element data are consistent with a simple model involving melting and igneous fractionation of AOA-like olivine to produce Type I chondrule olivine, but other data suggest that open-system melting of chondrules occurred in a different gaseous environment than that which produced AOAs.


## 1. INTRODUCTION

Most carbonaceous (C) chondrites contain lumpy, olivine-rich inclusions up to a few millimeters across known as amoeboid olivine aggregates (AOAs) (Grossman, 1974; Grossman and Steele, 1976; Grossman et al., 1979; Krot et al., 2004a) or amoeboid olivine inclusions (AOIs) (Rubin, 1998; Chizmadia et al., 2002), which formed primarily as aggregates of fine-grained condensates, with or without the involvement of sintering and small-scale melting (e.g., Grossman and Steele, 1976; Wark, 1979; Kornacki and Wood, 1984; Komatsu et al., 2001; Krot et al., 2004a,b,c; Weisberg et al., 2004; Scott and Krot, 2005; Sugiura et al., 2009). They contain variable proportions of different mineral assemblages that appear to record various formation conditions, including: (a) olivine + metal (e.g.,

* Corresponding author. Tel.: +1 503 725 3372; fax: +1 503 725 3025.

*E-mail address:* ruzickaa@pdx.edu (A. Ruzicka).

0016-7037/$ - see front matter © 2011 Elsevier Ltd. All rights reserved.
doi:10.1016/j.gca.2011.11.043

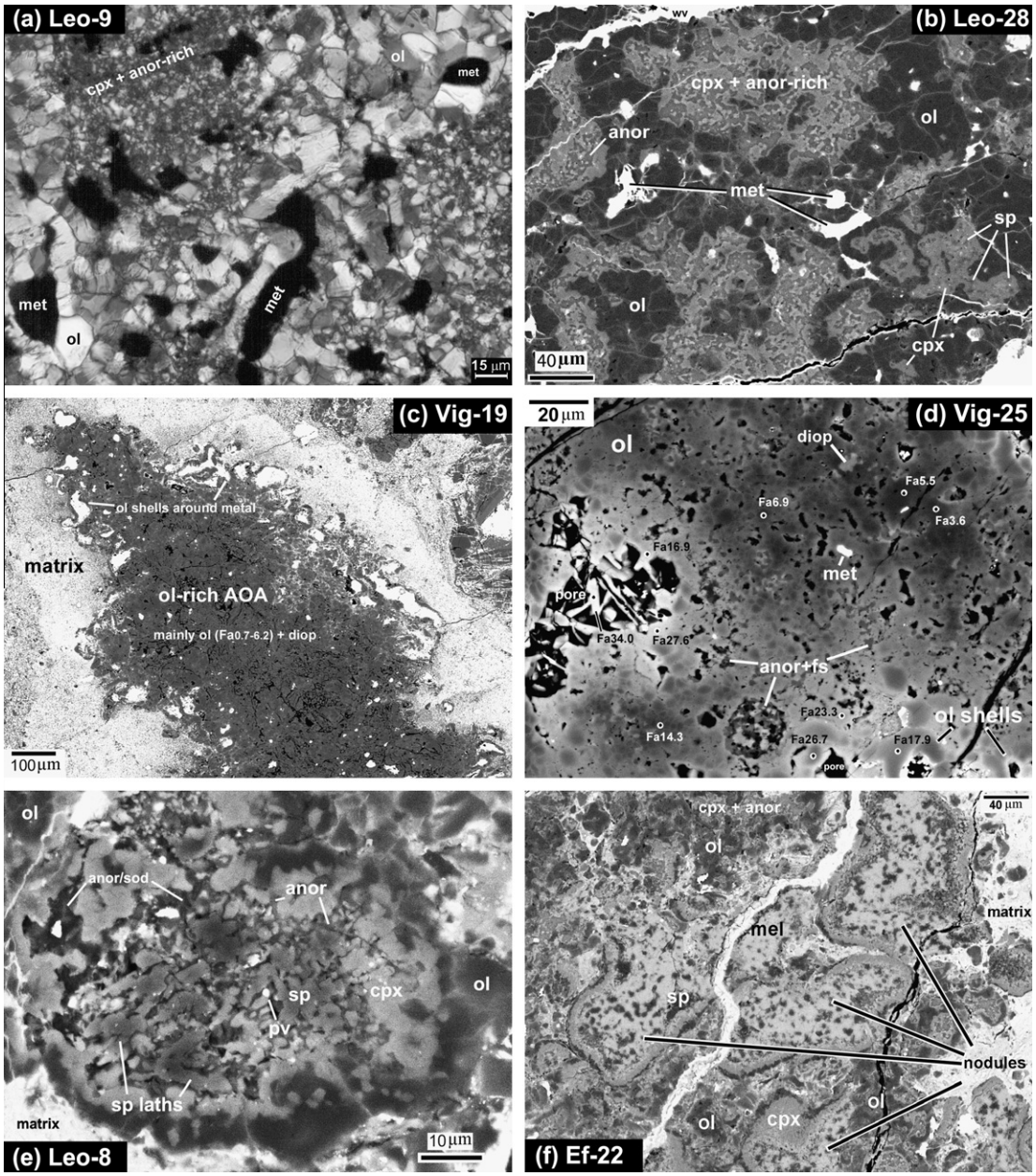


Fig. 1. Cross-polarized transmitted light (a) and BSE (b-l) images of AOAs from Efremovka (Ef), Leoville (Leo), and Vigarano (Vig). Mineral abbreviations: ol = olivine; diop = Al-diopside; cpx = Ca-rich pyroxene (diopside–fassaite); anor = anorthite; sod = sodalite; neph = nepheline; fs = feldspathoid; met = FeNi metal; sp = spinel; mel = melilite; pv = perovskite; lpx = low-Ca pyroxene, pl = plagioclase. (a) Ol-metal assemblage and cpx + anor patch in Leo-29, with atypically large ol grains meeting in triple junctions and forming shells around metal. (b) Ol-metal assemblage and cpx + anor patches in Leo-28. (c) Ol-rich AOA Vig-19 has a core rich in ol and cpx, and a periphery that includes metal grains surrounded by ol shells. (d) Ferrous ol associated with pores (black) in Vig-25, with ol forming shells around cavities (bottom center and bottom right) and tabular to acicular grains extending into and across cavities (left); feldspathoids are abundant. Spots show Fa values determined by EMPA. (e) Sp-rich nodule in Leo-8 with a core containing sp, cpx, and anor grading outwards into cpx and then ol. Some sp grains (dark) have lath-like crystal habit. (f) Mel + sp cored nodules in Ef-22, each surrounded by cpx layers grading outwards to ol; cpx + anor patches occur elsewhere (at top). The bright vein is filled with terrestrial weathering products. (g) Outer portion of Ef-12 showing opx (dark)-metal (white) patches separated by fine-grained ol, lpx, and anor. (h) Ef-8 has a typical AOA core (upper left), and an outer facies rich in low-Ca pyroxene. Most of the outer facies consists of fine-grained lpx, anor, and metal (bright); in some areas, lpx poikilitically encloses ol. Two sp-cored nodules (sp) surrounded by a layer of feldspathoid (dark) are visible. (i) Leo-10 has a core rich in granular ol and an edge composed of lpx that poikilitically encloses ol. (j) Portion of Ef-18 showing a granular-textured core rich in ol and lpx, and a surrounding lpx-rich edge facies; the latter contains portions rich in metal (bright) and low-Ca pyroxene (dark), and subcircular regions (at center left and upper left) with ol poikilitically enclosed by lpx. (k) Context image for Ef-11 showing a central lobe rich in sp and cpx, lobes rich in cpx and anor, and an ol-rich edge. The box shows the region magnified in part l. (l) Portion of inclusion Ef-11 showing ol-rich AOA facies and attached cpx + anor facies; the latter contains some sp-cored nodules (dark spots at right).

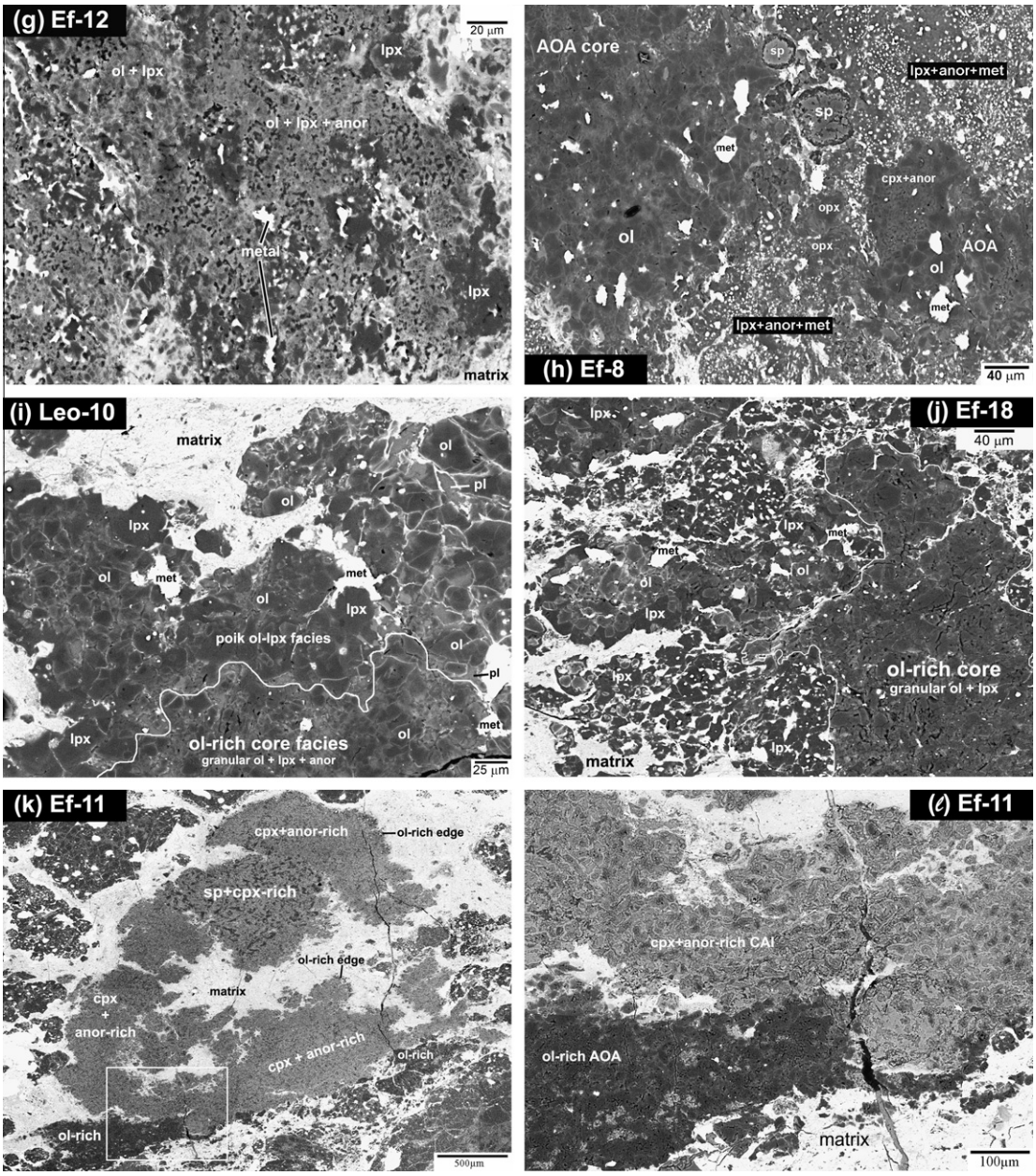


Fig. 1. *(continued)*

Komatsu et al., 2001; Weisberg et al., 2004); (b) spinel- or melilite-rich nodules and ribbons that have CAI-like mineralogies and which represent CAIs (e.g., Komatsu et al., 2001; Krot et al., 2004a); (c) Ca–Al–pyroxene + anorthite assemblages that may have formed by reaction of CAI constituents with nebular gas (Krot et al., 2004a,b,c, 2006); (d) low-Ca pyroxene assemblages that may represent condensation/reaction with nebular gas (Krot et al., 2004b, 2005); and (e) variable amounts of secondary minerals. It has been suggested that AOAs represent an intermediate stage in the development between early-formed refractory inclusions (CAIs) and later-formed chondrules (McSween, 1977; Wark, 1979; Krot et al., 2004a,b; Russell et al., 2006), and that AOAs may be related to the formation of Wark-Lovering rims on coarse-grained CAIs (Wark, 1979; Weisberg et al., 2004; Krot et al., 2004a). Their O-isotopic compositions suggest a close genetic link to CAIs (e.g., Hiyagon and Hashimoto, 1999; Krot et al., 2002; Aléon et al., 2002; Fagan et al., 2004; Weisberg et al., 2007; Yurimoto et al., 2008), and as with CAIs, they constitute an important class of distinctive material of solar nebula origin. However, some important issues concerning AOAs have not yet been fully resolved. Namely: (1) What processes were most important in forming AOAs, and under what conditions did they form? (2) Do AOAs truly represent an intermediate stage of development between CAIs and chondrules, and if so, how are these objects related?

We used optical light microscopy (OLM), scanning electron microscopy (SEM), electron microprobe analysis (EMPA), and secondary ion mass spectrometry (SIMS) to

Table 1
Samples included in study.[a]

| Meteorite | Source | PTS | Objects (AOAs except where noted) |
|---|---|---|---|
| Efremovka | AMNH | 4221-3 | Ef-1, Ef-2, Ef-3, Ef-4, Ef-5, Ef-6, Ef-7, Ef-8 |
| Efremovka | AMNH | 4221-2 | Ef-9, Ef-10$^{C}$, Ef-11$^{CA}$, Ef-12, Ef-13, Ef-14, Ef-14A, Ef-15, Ef-16, Ef-17, Ef-18, Ef-19, Ef-21 |
| Efremovka | USNM | 6456-2 | Ef-22, Ef-24, Ef-25B, Ef-26 |
| Leoville | AMNH | 4337-1 | Leo-1$^{C}$, Leo-1A$^{C}$, Leo-3, Leo-4, Leo-5$^{C}$, Leo-5A |
| Leoville | USNM | 3535-3 | Leo-6, Leo-7, Leo-8, Leo-9, Leo-10, Leo-11, Leo-12, Leo-13, Leo-14, Leo-15, Leo-17, Leo-18, Leo-19$^{C}$, Leo-20, Leo-21, Leo-22$^{C}$, Leo-23, Leo-24, Leo-25 |
| Leoville | AMNH | 4337-2 | Leo-27, Leo-28, Leo-29$^{CA}$, Leo-30, Leo-31 |
| Vigarano | AMNH | 2226-6 | Vig-1, Vig-2, Vig-3, Vig-4, Vig-5, Vig-6, Vig-8, Vig-9$^{C}$, Vig-10A$^{C}$, Vig-11$^{CA}$, Vig-12A, Vig-12B, Vig-12C$^{C}$, Vig-13, Vig-14, Vig-15, Vig-16 |
| Vigarano | AMNH | 2226-9 | Vig-17, Vig-18, Vig-19$^{C}$, Vig-21, Vig-22, Vig-23, Vig-24$^{C}$ |
| Vigarano | CML | 0377-1 | Vig-25, Vig-25A, Vig-26, Vig-28, Vig-29, Vig-30, Vig-31, Vig-32, Vig-33, Vig-34, Vig-37, Vig-38, Vig-39, Vig-40, Vig-41, Vig-42 |

[a] AMNH = American Museum of Natural History, USNM = U.S. National Museum, CML = Cascadia Meteorite Laboratory, PTS = polished thin section, $^{C}$CAI, $^{CA}$CAI-AOA composite object. Some of the same sections were studied by Ruzicka (1996), but there is no correspondence between the object designations in that work and this table.

analyze AOAs in three reduced CV3 meteorites (Leoville, Vigarano, Efremovka). The AOAs in these CV3 chondrites contain minor secondary phases and are believed to be mineralogically more pristine than those in the oxidized Allende-like CV3 chondrites (Komatsu et al., 2001; Fagan et al., 2004), making them attractive for further study. These meteorites, however, experienced variable degrees of mild metamorphism and aqueous alteration, corresponding to subtypes of 3.1–3.4 (Bonal et al., 2006), which resulted in modified mineral compositions (Komatsu et al., 2001) and possibly oxygen isotope compositions (Fagan et al., 2004). Vigarano is a breccia containing both reduced and oxidized components (a mixture of $CV_R$ and $CV_{OXA}$) of presumed different alteration histories (Krot et al., 2000a). Although limited SIMS and Laser Ablation-Inductively Coupled Plasma-Mass Spectrometry (LA-ICP-MS) chemical data for AOAs were reported by Weisberg et al. (1991) and by Russell et al. (2003), this work is the first to involve significant *in situ* trace-element analyses of AOA constituents. Preliminary data were reported by Ruzicka et al. (2008a).

## 2. SAMPLES AND METHODS

Table 1 provides information about the thin sections and objects that were studied. Objects of interest in the sections were identified and characterized at Portland State University (PSU), Portland, Oregon, employing OLM techniques using a Leica DM2500 petrographic microscope, and backscattered electron (BSE) imaging using a JEOL JSM-35C SEM. Petrographic data were used to select areas for subsequent *in situ* chemical analyses. EMPA was used to analyze major- and minor-elements using a Cameca SX-100 electron microprobe at Oregon State University, Corvallis, Oregon, via remote access from PSU. Trace elements were analyzed by SIMS using the modified Cameca ims-3f ion microprobe at Washington University. Both EMPA and SIMS analyses were obtained using "narrow-beam" (1-μm-diameter EMPA, 15–20-μm-diameter SIMS) and "broad-beam" (40–50-μm-diameter EMPA and SIMS) conditions. As the inclusions that were studied are fine-grained (with grain diameters typically <5–10 μm), broad-beam analyses provide estimates of bulk compositions, both for different zones within objects and for the objects overall. Broad or 'defocused' beam EMPA data (DB-EMPA) for inclusions were obtained using a combination of grid patterns, traverses, and targeted analyses in the inclusions. DB-EMPA analytical totals were often low owing to the presence of voids in the analyzed volumes; bulk compositions for inclusions obtained by averaging individual analyses had totals between 96–102 wt.% (90–100 wt.% for the often more porous inclusions in Vigarano). Mineral proportions were calculated for each DB-EMPA analysis using a norm calculation that was tailored to AOAs. For comparison to AOA data, a version of the CWPI thermodynamic code (Petaev and Wood, 1998, 2005) was used to model equilibrium condensate compositions. All CI-normalized plots utilize the average CI chondrite data of Anders and Grevesse (1989). Plots showing elements arranged by condensation temperatures are based on the work of Lodders (2003), except that the relative order of condensation temperatures for Na and K were switched consistent with results from the CWPI program. Further details on experimental methods are given in the Appendix.

## 3. RESULTS

Representative images for inclusions are shown in Fig. 1, and chemical data (SIMS, EMPA, DB-EMPA) are given in Tables 2–5.

### 3.1. Petrography

AOAs in Efremovka, Leoville and Vigarano contain variable proportions of different assemblages, including the following. *Olivine + metal assemblages* are composed of fine-grained olivine grains (typically ~5–10 μm in diameter), which often meet in triple junctions or that form polygranular shells on metal grains (Fig. 1a–c). Metal-rich peripheries for AOAs are common (Fig. 1c). C*a-rich pyroxene + anorthite* (*cpx + anor*) *patches* consist of finely intergrown pyroxene (Al-diopside to 'fassaite') and anorthite that have convolute margins between the two, sometimes

Table 2
Bulk compositions and norms of AOAs and their components determined by DB-EMPA.[a]

| | Median AOA | Mean AOA, Efremovka | Mean AOA, Leoville | Mean AOA, Vigarano | Mean cpx + anor-rich area | Mean sp-rich nodule | Ef-11 cpx + anor facies | Ef-11 ol facies (AOA) | Leo-29 sp + mel facies (CAI) | Leo-29 ol facies (AOA) | Ef-22 mel-bearing AOA | Ef-12 lpx bearing AOA | Ef-15 Mn-rich AOA |
|---|---|---|---|---|---|---|---|---|---|---|---|---|---|
| *N* | 48 | 15 | 15 | 18 | 10 | 7 | 8 | 9 | 6 | 9 | 38 | 18 | 21 |
| *Wt.%* | | | | | | | | | | | | | |
| $SiO_2$ | 38.6 | 40.3 | 39.5 | 35.8 | 39.3 | 11.9 | 40.4 | 49.0 | 15.8 | 39.6 | 38.7 | 41.3 | 39.9 |
| $Al_2O_3$ | 6.11 | 6.17 | 6.87 | 8.98 | 19.0 | 53.7 | 25.2 | 1.83 | 48.4 | 3.15 | 12.7 | 4.76 | 4.53 |
| $Cr_2O_3$ | 0.22 | 0.29 | 0.23 | 0.20 | 0.19 | 0.39 | 0.14 | 0.26 | 0.13 | 0.27 | 0.27 | 0.29 | 0.37 |
| MnO | 0.09 | 0.16 | 0.08 | 0.09 | 0.04 | 0.03 | 0.02 | 0.11 | <0.01 | 0.04 | 0.19 | 0.14 | 0.62 |
| MgO | 39.3 | 41.0 | 39.2 | 32.7 | 24.0 | 18.7 | 13.1 | 49.6 | 14.0 | 43.4 | 30.9 | 41.3 | 41.1 |
| CaO | 3.67 | 4.14 | 4.65 | 5.04 | 11.9 | 6.38 | 17.8 | 1.27 | 18.4 | 1.32 | 8.74 | 2.76 | 2.94 |
| $Na_2O$ | 0.07 | 0.10 | 0.11 | 0.80 | 0.15 | 0.46 | 0.14 | 0.06 | 0.06 | 0.01 | 0.18 | 0.13 | 0.05 |
| Cl | 0.02 | 0.02 | 0.01 | 0.11 | 0.01 | 0.02 | 0.02 | 0.01 | 0.02 | 0.01 | 0.02 | 0.02 | 0.02 |
| S | 0.08 | 0.11 | 0.09 | 0.18 | 0.07 | 0.03 | 0.01 | 0.02 | 0.05 | 0.06 | 0.03 | 0.08 | 0.04 |
| Ni | 0.23 | 0.20 | 0.35 | 0.23 | 0.20 | 0.06 | 0.03 | 0.04 | 0.04 | 0.25 | 0.16 | 0.15 | 0.31 |
| Fe sulf | 0.13 | 0.20 | 0.16 | 0.31 | 0.12 | 0.06 | 0.02 | 0.03 | 0.09 | 0.10 | 0.05 | 0.14 | 0.07 |
| Fe met | 1.99 | 1.71 | 3.23 | 2.07 | 0.19 | 0.02 | n.d. | 0.19 | <0.01 | 2.55 | 1.54 | 1.64 | 3.11 |
| FeO | 3.43 | 3.71 | 2.18 | 7.72 | 3.68 | 4.34 | 1.39 | 3.11 | 0.37 | 0.41 | 3.40 | 4.75 | 5.11 |
| Total | 94.0 | 98.1 | 96.6 | 94.2 | 99.0 | 96.1 | 98.2 | 97.6 | 97.3 | 96.1 | 96.9 | 97.4 | 98.2 |
| *Vol.%* | | | | | | | | | | | | | |
| Olivine | 78.4 | 72.9 | 68.4 | 67.6 | 36.7 | 7.37 | 8.99 | 91.3 | 10.3 | 86.2 | 54.0 | 73.1 | 77.7 |
| Cpx | 8.28 | 7.95 | 8.44 | 13.8 | 21.7 | 14.7 | 47.6 | 3.22 | 24.9 | 2.03 | 7.55 | 1.59 | 2.09 |
| Anor | 7.47 | 11.2 | 12.7 | 5.02 | 33.0 | 9.47 | 24.7 | 2.36 | <0.01 | 4.96 | 25.1 | 13.9 | 14.3 |
| Lpx | 3.46 | 5.16 | 6.40 | 2.88 | 4.48 | 3.08 | 17.8 | 2.69 | 0.43 | 4.29 | 2.88 | 9.49 | 4.06 |
| Metal | 1.04 | 0.92 | 1.51 | 1.05 | 0.70 | 0.12 | n.d. | 0.08 | <0.01 | 1.12 | 0.81 | 0.72 | 1.45 |
| Spinel | 0.71 | 1.04 | 1.02 | 3.23 | 2.53 | 62.3 | 0.18 | 0.02 | 41.6 | 1.17 | 2.86 | 0.40 | 0.15 |
| Neph | 0.29 | 0.49 | 0.58 | 3.23 | 0.76 | 2.62 | 0.60 | 0.27 | 0.10 | 0.03 | 0.83 | 0.63 | 0.11 |
| Troilite | 0.17 | 0.23 | 0.19 | 0.39 | 0.13 | 0.07 | 0.01 | 0.04 | 0.11 | 0.11 | 0.05 | 0.16 | 0.08 |
| Sod | 0.13 | 0.12 | 0.07 | 0.87 | 0.06 | 0.22 | 0.15 | 0.06 | 0.17 | 0.05 | 0.15 | 0.13 | 0.14 |
| Melilite | <0.01 | 0.41 | 0.61 | 1.95 | n.d. | <0.01 | n.d. | n.d. | 22.3 | n.d. | 5.78 | n.d. | n.d. |
| *At.* | | | | | | | | | | | | | |
| Mg# | 0.95 | 0.95 | 0.97 | 0.88 | 0.96 | 0.89 | 0.94 | 0.97 | 0.96 | 0.99 | 0.94 | 0.94 | 0.93 |
| Mg/Al | 7.92 | 8.78 | 7.13 | 4.61 | 1.74 | 0.44 | 0.66 | 34.2 | 0.37 | 19.4 | 3.07 | 11.0 | 11.5 |
| Si/Al | 5.41 | 5.80 | 4.83 | 3.39 | 1.88 | 0.20 | 1.36 | 19.0 | 0.28 | 10.6 | 2.58 | 7.35 | 7.48 |

[a] Abbreviations: *N* = number of objects included in median or mean, or number of analyses for region in individual objects, ol = olivine, cpx = Ca-rich pyroxene, anor = anorthite, sp = spinel, lpx = low-Ca pyroxene (normative enstatite + ferrosilite in most inclusions, confirmed low-Ca pyroxene in Ef-12), mel = melilite, sulf = sulfide (troilite), met = FeNi metal, neph = nepheline, sod = sodalite.

Table 3
Composition of bulk constituents in AOAs determined by broad beam SIMS.[a]

| Assemblage | Ol-rich[b] | Common cpx + anor[c] | Group II cpx + anor | Group II cpx + anor | Group II sp + cpx | Group II sp + cpx | Sp-rich | Sp-rich | Mel-rich | Mel-rich |
|---|---|---|---|---|---|---|---|---|---|---|
| Analysis | Mean (*s.d.*) | Mean (*s.d.*) | E1-B3 | E2-B2 | E11-B5a | V41-B2 | L11-B2 | L29-B2 | E9-B4 | E22-B1 |
| Na, mg/g | 0.101 (*0.067*) | 1.63 (*2.47*) | 7.21 | 1.11 | 1.29 | 3.02 | 0.155 | 0.136 | 0.560 | 0.103 |
| Mg, wt.% | 28.4 (*0.6*) | 16.3 (*6.3*) | 5.96 | 19.7 | 11.6 | 11.9 | 9.62 | 14.1 | 7.79 | 5.65 |
| Al, wt.% | 0.153 (*0.088*) | 7.52 (*3.99*) | n.a. | n.a. | n.d. | 20.9 | n.d. | n.d. | 28.8 | n.d. |
| Si, wt.% | 19.0 (*0.4*) | 19.0 (*1.4*) | 19.7 | 16.8 | 16.9 | 10.0 | 5.08 | 1.01 | 6.11 | 9.00 |
| P, μg/g | 109 (*80*) | 140 (*81*) | 33.0 | 151 | 61.7 | 218 | 195 | 50.9 | 89.8 | 46.4 |
| K, μg/g | 50.2 (*37.4*) | 392 (*1989*) | 282 | 92.2 | 414 | 308 | 191 | 182 | 227 | 46.0 |
| Ca, mg/g | 1.40 (*0.48*) | 58.4 (*32.9*) | 113 | 26.0 | 116 | 52.6 | 35.5 | 54.0 | 110 | 209 |
| Sc, μg/g | 2.67 (*1.17*) | 37.7 (*24.9*) | 10.8 | 6.95 | 16.8 | 32.3 | 227 | 47.8 | 18.1 | 103 |
| Ti, mg/g | 0.171 (*0.082*) | 3.77 (*2.50*) | 2.17 | 3.27 | 3.85 | 9.96 | 47.5 | 31.4 | 1.45 | 5.45 |
| V, μg/g | 49.4 (*26.4*) | 279 (*142*) | 211 | 277 | 1720 | 673 | 2520 | 3200 | 669 | 929 |
| Cr, mg/g | 1.27 (*0.61*) | 1.26 (*0.60*) | 0.828 | 1.81 | 2.35 | 0.849 | 0.340 | 0.431 | 0.309 | 0.218 |
| Mn, mg/g | 0.652 (*0.531*) | 0.518 (*0.511*) | 0.101 | 1.24 | 0.151 | 0.584 | 0.141 | 0.0959 | 0.0560 | 0.0672 |
| Fe, wt.% | 3.10 (*1.35*) | 4.56 (*2.94*) | 2.41 | 6.64 | 1.37 | 8.35 | 7.31 | 0.155 | 0.472 | 0.131 |
| Co, μg/g | 86.3 (*52.4*) | 163 (*125*) | 85.8 | 237 | 47.1 | 158 | 247 | 17.2 | 9.16 | 14.0 |
| Ni, μg/g | 0.127 (*0.148*) | 0.262 (*0.226*) | 0.0509 | 0.114 | 0.0479 | 0.0601 | 0.503 | 0.0928 | 0.0198 | 0.0620 |
| Rb, μg/g | 0.285 (*0.195*) | 1.68 (*6.90*) | n.d. | 0.735 | n.d. | 1.98 | 2.15 | 1.18 | 1.05 | 0.390 |
| Sr, μg/g | 1.04 (*0.62*) | 53.8 (*30.9*) | 155 | 22.0 | 157 | 31.1 | 49.2 | 50.6 | 75.7 | 133 |
| Y, μg/g | 0.575 (*0.384*) | 12.4 (*8.0*) | 0.684 | 0.809 | 0.670 | 2.34 | 146 | 29.3 | 30.8 | 22.0 |
| Zr, μg/g | 1.62 (*0.96*) | 38.3 (*26.2*) | 1.01 | 1.27 | 3.01 | 10.5 | 412 | 78.8 | 19.5 | 50.0 |
| Ba, μg/g | 0.722 (*0.434*) | 12.0 (*8.0*) | 13.1 | 4.01 | 47.2 | 33.9 | 6.28 | 3.61 | 2.93 | 4.14 |
| La, ng/g | 122 (*70*) | 1570 (*830*) | 604 | 265 | 3280 | 8890 | 21,800 | 48,700 | 9460 | 4120 |
| Ce, ng/g | 254 (*132*) | 4180 (*2320*) | 3710 | 1930 | 6420 | 18,900 | 77,200 | 72,900 | 9700 | 12,200 |
| Pr, ng/g | 35.7 (*20.5*) | 635 (*368*) | 487 | 161 | 1350 | 2860 | 10,300 | 14,600 | 2140 | 1500 |
| Nd, ng/g | 156 (*105*) | 3100 (*1930*) | 1410 | 494 | 6180 | 819 | 43,500 | 86,200 | 16,700 | 7690 |
| Sm, ng/g | 44.9 (*47.1*) | 1010 (*640*) | 818 | 263 | 2120 | 270 | 14,700 | 19,600 | 3550 | 2440 |
| Eu, ng/g | 7.53 (*4.67*) | 253 (*98*) | 274 | 103 | 752 | 87.0 | 845 | 689 | 638 | 1130 |
| Gd, ng/g | 51.0 (*37.7*) | 1390 (*940*) | 133 | 96.6 | 360 | 310 | 14,600 | 53,000 | 5740 | 2160 |
| Tb, ng/g | 11.2 (*9.1*) | 274 (*178*) | 30.2 | 12.4 | 56.2 | 56.7 | 2650 | 7400 | 898 | 432 |
| Dy, ng/g | 71.1 (*54.6*) | 1890 (*1250*) | 179 | 138 | 328 | 468 | 21,800 | 32,200 | 5550 | 3210 |
| Ho, ng/g | 16.6 (*11.7*) | 407 (*278*) | 31.9 | 18.6 | 34.5 | 94.3 | 5280 | 2130 | 863 | 610 |
| Er, ng/g | 60.6 (*38.9*) | 1270 (*840*) | 61.6 | 86.3 | 64.3 | 273 | 13,000 | 2680 | 2530 | 2080 |
| Tm, ng/g | 9.63 (*8.80*) | 188 (*124*) | 165 | 45.5 | 293 | 57.0 | 2020 | 1760 | 704 | 230 |
| Yb, ng/g | 77.0 (*43.9*) | 1380 (*1000*) | 1310 | 1050 | 667 | 381 | 15,100 | 4340 | 459 | 1850 |
| Lu, ng/g | 16.4 (*11.6*) | 204 (*160*) | 17.9 | 25.6 | 12.6 | 58.6 | 1780 | 174 | 473 | 375 |

[a] Abbreviations as in Table 2, also s.d. = standard deviation, n.a. = not analyzed, n.d. = not determined. Analysis designations: characters before hyphen refer to meteorite (E = Efremovka, L = Leoville, V = Vigarano) and inclusion number, characters after hyphen refer to analysis number.
[b] Based on 12 analyses.
[c] Based on 22 analyses.

with pyroxene forming "islands" within anorthite (Fig. 1b). Spinel is a common accessory phase. *Spinel- or melilite-rich* (*sp + mel*) *nodules and ribbons* mostly have cores rich in spinel, although some are rich in melilite; perovskite and hibonite are accessory minerals (Fig. 1e–f). The cores are surrounded by layers of Ca-pyroxene with or without anorthite (Fig. 1e–f). In detail, some spinel grains show a lath-like or prismatic morphology, possibly a pseudomorph of hibonite (Fig. 1e). These objects have CAI-like mineralogies and clearly represent CAIs (e.g., Komatsu et al., 2001; Krot et al., 2004a). *Low-Ca pyroxene assemblages* vary in their textures. Low-Ca pyroxene was confirmed in four inclusions (Ef-8, Ef-12, Ef-18, Leo-10). These objects are discussed in more detail as they appear to be transitional between typical AOAs and chondrules.

Inclusion Ef-12 contains low-Ca pyroxene within the inclusion, mainly towards the periphery, where the largest pyroxene grains surround metal grains, in clumps that are separated by fine-grained and somewhat porous olivine, anorthite, and low-Ca pyroxene (Fig. 1g). Elsewhere, Ef-12 is rich in fine grained olivine and contains cpx + anor patches that include spinel, making it clear that this object is truly an AOA.

Ef-8 has a typical AOA core rich in olivine that contains cpx + anor patches, and a distinctly different outer zone that contains normative low-Ca pyroxene (~52 vol.%), olivine (~16%), anorthite (15%), clinopyroxene (~8%), metal (~5%), and troilite (~2%) (Fig. 1h). Two spinel-cored nodules occur close to the contact of the core and outer zone, and a separate, smaller AOA appears to be embedded within the outer zone (Fig. 1h). In addition, the outer zone contains subcircular, metal-poor regions with low-Ca pyroxene poikilitically enclosing olivine in a texture reminiscent of chondrules.

Leo-10 and Ef-18 contain cores of granular olivine + low-Ca pyroxene ± anorthite that are surrounded

Table 4
Compiled data for the composition of olivine in AOAs from Efremovka, Leoville, and Vigarano as determined by electron microprobe.[a]

| | Forsterite, normal Mn[b] | | Magnesian, normal Mn[c] | | FeO-rich, normal Mn[d] | | MnO-rich[e] | |
|---|---|---|---|---|---|---|---|---|
| | Mean | s.d. | Mean | s.d. | Mean | s.d | Mean | s.d. |
| *Wt%* | | | | | | | | |
| $SiO_2$ | 42.4 | 0.4 | 41.5 | 0.6 | 38.1 | 1.4 | 40.9 | 0.9 |
| $TiO_2$ | 0.03 | 0.03 | 0.03 | 0.03 | 0.05 | 0.04 | 0.01 | 0.02 |
| $Al_2O_3$ | 0.14 | 0.09 | 0.22 | 0.20 | 0.27 | 0.24 | 0.23 | 0.21 |
| $Cr_2O_3$ | 0.14 | 0.09 | 0.11 | 0.09 | 0.17 | 0.17 | 0.14 | 0.12 |
| FeO | 0.58 | 0.23 | 3.85 | 2.22 | 20.5 | 7.0 | 7.44 | 3.28 |
| MnO | 0.05 | 0.05 | 0.14 | 0.14 | 0.21 | 0.08 | 1.05 | 0.16 |
| MgO | 55.8 | 0.7 | 53.2 | 1.9 | 39.8 | 5.7 | 49.6 | 2.9 |
| CaO | 0.17 | 0.18 | 0.18 | 0.15 | 0.22 | 0.31 | 0.20 | 0.11 |
| $Na_2O$ | 0.01 | 0.01 | 0.01 | 0.01 | 0.04 | 0.05 | 0.01 | 0.01 |
| NiO | 0.03 | 0.04 | 0.09 | 0.11 | 0.10 | 0.09 | 0.08 | 0.08 |
| Total | 99.4 | | 99.4 | | 99.4 | | 99.7 | |
| *Mol%* | | | | | | | | |
| Fa | 0.58 | 0.23 | 3.9 | 2.3 | 22.7 | 8.5 | 7.8 | 3.7 |

[a] s.d. = standard deviation.
[b] Olivine with Fa 0–1 mol% (44 analyses).
[c] Olivine with Fa 1–10 mol% and MnO <0.7 wt.% (280 analyses).
[d] Olivine with Fa >10 mol% and MnO <0.7 wt.% (62 analyses).
[e] Olivine with MnO >0.7 wt.% (11 analyses).

Table 5
Composition of minerals in AOAs determined by narrow beam SIMS.[a]

| Phase/analysis | Olivine[b] | Olivine, Mn-P-rich | Ca-rich pyroxene | Ca-rich pyroxene | Ca-rich pyroxene | Low-Ca pyroxene | Spinel | Melilite | Melilite |
|---|---|---|---|---|---|---|---|---|---|
| | Mean (*s.d.*) | E2-2 | E9-2 | E14-2 | E22-3 | L10-4 | V41-2 | E22-1 | L11-1 |
| Na, mg/g | 0.185 (*0.168*) | 0.313 | 0.412 | 0.498 | 0.161 | 0.276 | 2.29 | 0.565 | 0.633 |
| Mg, wt.% | 25.0 (*1.0*) | 23.4 | 11.5 | 9.90 | 7.22 | 17.3 | 15.9 | 1.31 | 3.75 |
| Al, wt.% | 0.153 (*0.129*) | 0.184 | 8.07 | 5.35 | 13.1 | 1.12 | 33.4 | 25.5 | 29.0 |
| Si, wt.% | 19.2 (*0.7*) | 19.2 | 21.9 | 22.9 | 19.8 | 26.5 | 2.04 | 11.3 | 11.3 |
| P, μg/g | 126 (*122*) | 1290 | 473 | 716 | 120 | 75.7 | 12.8 | 57.5 | 436 |
| K, μg/g | 84.4 (*60.3*) | 138 | 209 | 325 | 104 | 171 | 664 | 193 | 363 |
| Ca, mg/g | 1.06 (*0.40*) | 2.60 | 91.2 | 105 | 113 | 7.10 | 5.92 | 296 | 253 |
| Sc, μg/g | 2.83 (*1.47*) | 2.41 | 41.7 | 29.4 | 126 | 19.9 | 6.68 | 24.8 | 29.2 |
| Ti, mg/g | 0.113 (*0.053*) | 0.0650 | 3.38 | 2.21 | 22.9 | 1.27 | 3.85 | 1.99 | 3.50 |
| V, μg/g | 40.7 (*19.4*) | 20.2 | 434 | 159 | 1540 | 123 | 1890 | 141 | 510 |
| Cr, mg/g | 1.09 (*0.59*) | 1.69 | 1.58 | 0.439 | 0.773 | 3.26 | 2.20 | 0.189 | 0.170 |
| Mn, mg/g | 0.600 (*0.477*) | 3.16 | 0.673 | 0.109 | 0.112 | 0.445 | 0.210 | 0.0932 | 0.0882 |
| Fe, wt.% | 3.66 (*5.43*) | 6.12 | 2.46 | 2.26 | 0.783 | 0.792 | 3.84 | 0.256 | 0.327 |
| Co, μg/g | 74.5 (*68.5*) | 162 | 90.2 | 105 | 66.3 | 44.0 | 23.0 | 53.1 | 23.3 |
| Ni, μg/g | 607 (*424*) | 1830 | 2720 | 1120 | 2100 | 592 | n.d. | 555 | 539 |
| Rb, μg/g | 0.423 (*0.448*) | 0.467 | 0.856 | 0.186 | 0.547 | 0.616 | 1.50 | n.d. | n.d. |
| Sr, μg/g | 1.18 (*0.99*) | 3.28 | 29.2 | 76.1 | 39.4 | 1.25 | 72.0 | 144 | 168 |
| Y, μg/g | 0.354 (*0.203*) | 0.131 | 13.1 | 10.1 | 59.7 | 0.814 | 0.663 | 17.7 | 22.6 |
| Zr, μg/g | 1.82 (*1.50*) | 1.33 | 32.1 | 20.2 | 235 | 2.21 | 7.58 | 13.1 | 19.2 |
| Ba, μg/g | 0.662 (*0.417*) | 2.65 | 1.21 | 2.37 | 2.82 | 1.33 | 78.0 | 6.32 | 17.1 |
| La, ng/g | 212 (*130*) | 540 | 2070 | 1670 | 3540 | 106 | 1470 | 5840 | 6340 |
| Ce, ng/g | 253 (*126*) | 452 | 5920 | 5180 | 15,400 | 174 | 3490 | 24,300 | 14,000 |
| Pr, ng/g | 42.1 (*28.2*) | 68.6 | 641 | 620 | 1810 | 25.2 | 310 | 2300 | 2570 |

[a] Abbreviations as in Tables 2 and 3.
[b] Based on 18 analyses; excludes E2-2.

by peripheries rich in low-Ca pyroxene (Fig. 1i and j). In both objects, low-Ca pyroxene in the peripheral regions poikilitically encloses olivine in a texture reminiscent to that in chondrules. In Ef-18, some subcircular regions in the periphery have a high proportion of olivine and a small proportion of metal; other more irregularly-shaped regions have a higher proportion of metal and a smaller proportion of olivine (Fig. 1j). Neither Leo-10 nor Ef-18 contain spinel

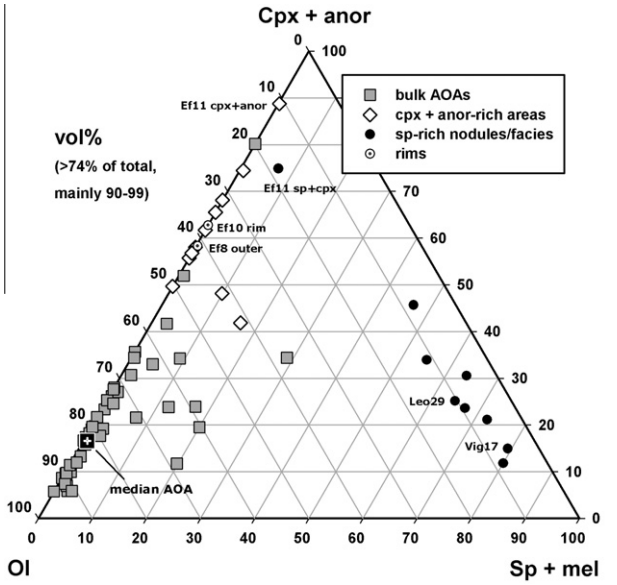


Fig. 2. Ternary diagram illustrating the normative mineralogy of AOAs and some of their components as determined by DB-EMPA. Mineral abbreviations as in Fig. 1.

nor the cpx + anor assemblages of most AOAs, raising the possibility that they are not AOAs. However, they have cores texturally similar to AOAs and peripheries that could represent melted regions analogous to chondrules.

Some of the AOAs we studied form composite objects with fine-grained, spinel-rich CAIs and appear to be transitional between AOAs and CAIs. The best examples of these are given by inclusions Ef-11 and Leo-29.

Ef-11 is a remarkable large inclusion (~3.3 × 2.1 mm across) that has three distinct mineral facies present in different lobes (Fig. 1k). A "central" lobe (⩾1 mm across) is composed of spinel-cored nodules with intervening Ca-pyroxene layers (sp + cpx facies) and is a typical fine-grained, spinel-rich CAI. On opposite sides of this lobe are two lobes that are composed mainly of a fine-grained intergrowth of Ca-pyroxene and anorthite with a texture similar to cpx + anor patches but occurring over a larger region (the cpx + anor facies, Fig. 1k and l). Still farther from the center of the inclusion is a lobe (~0.5 × 1 mm) composed of an AOA (Fig. 1k and l). Elsewhere, olivine grains of similar composition to that in the AOA lobe are adhered to the outer edge of the cpx + anor-rich facies in different locations (Fig. 1k).

Leo-29 is another composite inclusion (<0.4 × 2.3 mm across), consisting of an olivine-rich AOA (⩽0.4 × 0.6 mm) that is attached to a fine-grained CAI (<0.4 × 1.4 mm) containing spinel-cored nodules, which are surrounded by successive melilite and thin anorthite and rare clinopyroxene layers. Perovskite inclusions occur within the spinel.

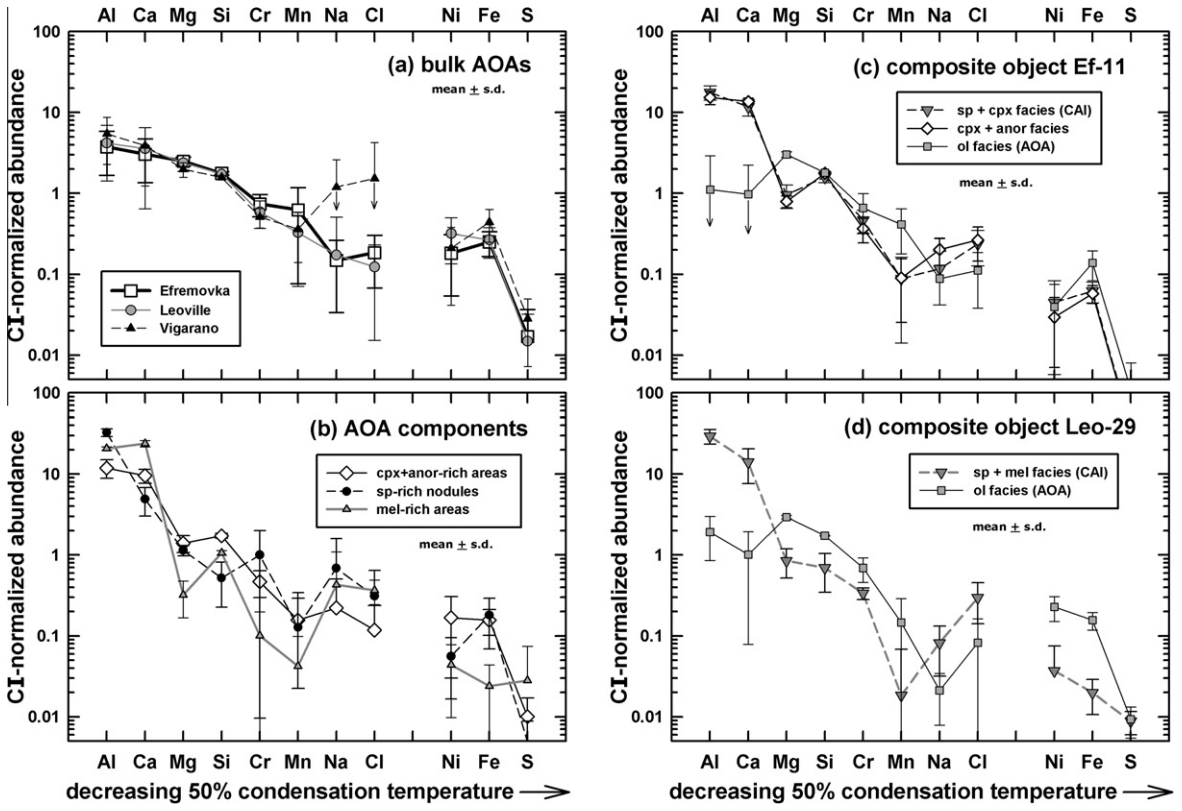


Fig. 3. Plot showing CI-normalized abundances of AOAs and their components determined by DB-EMPA. Points show mean values, bars standard deviations of means. (a) Bulk AOAs in Efremovka, Leoville, and Vigarano. (b) Al-rich components in AOAs. (c) Different regions in composite inclusion Ef-11. (d) Different regions in composite inclusion Leo-29. Mineral abbreviations as in Fig. 1.

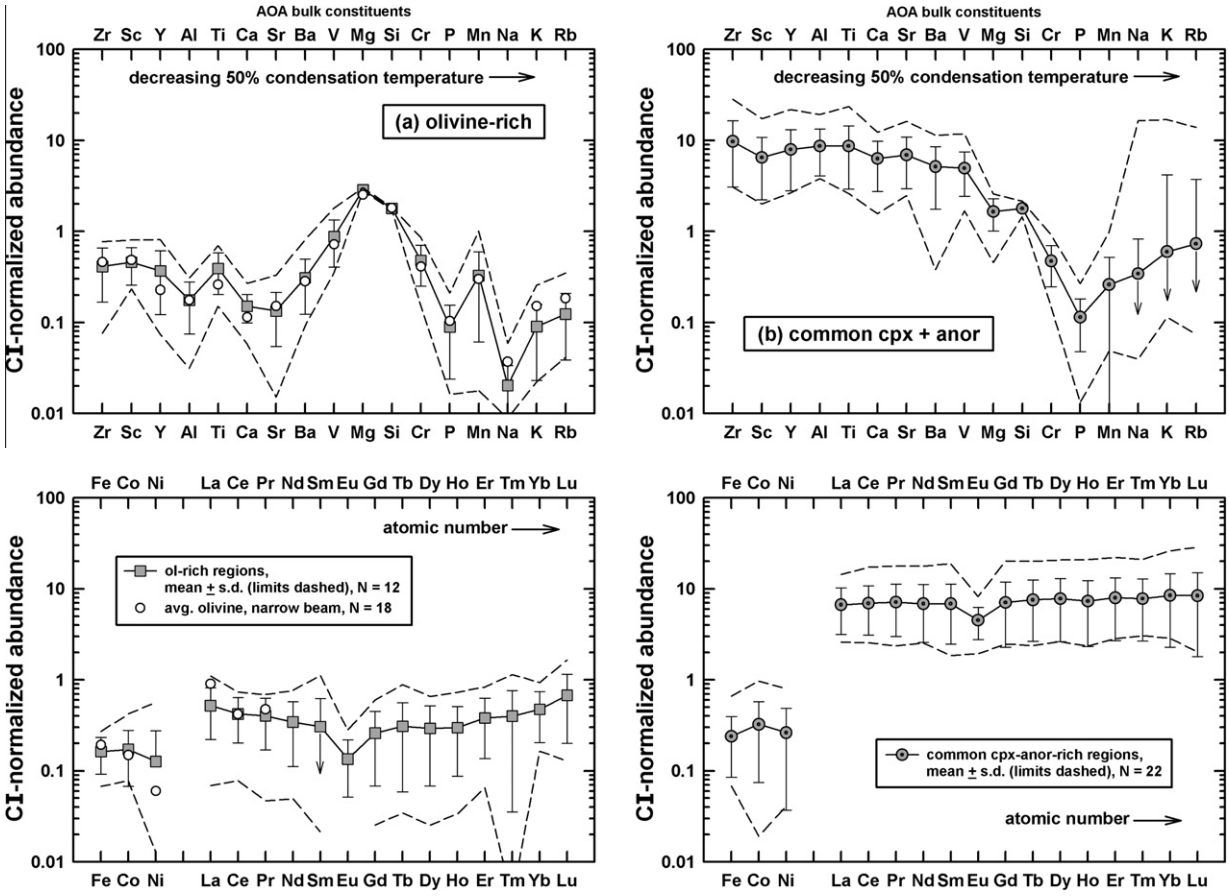


Fig. 4. Plot showing CI-normalized abundances for bulk constituents in AOAs determined by broad beam SIMS. (a) Ol-rich regions. Points show mean values, bars standard deviations, dashes compositional ranges; $N$ = number of analyses. (b) Analyses of cpx + anor areas showing the 'common' refractory trace element signature are characterized by relatively uniform enrichments in elements more refractory than Mg. Symbols are the same as in Fig. 4a. (c) Analyses of cpx or anor-rich regions showing a 'Group II' signature are characterized by depletions of the most refractory elements (Zr, Sc, Y, many HREE) relative to somewhat less refractory elements (Al-V, LREE). (d) Analyses of sp + cpx areas in three inclusions show a Group II signature. (e) Analyses of sp-rich nodules. (f) Analyses of a mel-rich nodule (E22-B1) and ribbon (E9-B4). (g) Analyses of AOA core (E8-B1, E8-B3) and lpx + anor-rich outer facies (E8-B2). Mineral abbreviations as in Fig. 1.

Fig. 2 shows a ternary diagram illustrating the normative proportions of the olivine, Ca-pyroxene + anorthite, and spinel + melilite assemblages. Most bulk AOAs lie close to the olivine – Ca-pyroxene + anorthite join and are dominated by olivine (~65–95 vol.%) although they show significant variation in the amount of these components. The spinel + melilite 'CAI' component predominates in spinel-rich nodules (45–80 vol.%), and although this component can be volumetrically significant in bulk AOAs (up to 30 vol.%), in most inclusions it is present at the <5 vol.% level (Fig. 2).

Although AOAs in Efremovka, Leoville and Vigarano largely escaped secondary mineralization and typically contain <1% feldspathoid minerals, such mineralization was more prevalent in some inclusions from Vigarano. In addition, one inclusion in Leoville (Leo-17) appears to have been heavily altered: it shows an AOA-like structure with spinel-cored nodular bodies and cpx + anor patches, but olivine has been largely replaced with a ferromagnesian material that gives low EMPA analysis totals (~95–96 wt.%) and which is likely hydrated. Commonly in Vigarano AOAs, metal was altered to oxidized material, or was removed entirely to form pores. This left behind olivine shells that encircle oxidized metal or pores (Fig. 1d). Some of the larger pores are partly filled with elongate to acicular ferrous olivine grains that appear to have grown into, and even across, the cavities (Fig. 1d). Other Vigarano inclusions contain magnesian olivine in sharp contact with ferrous matrix olivine with no evidence for chemical exchange between the two. Our data support the idea that Vigarano in particular contains material with a wide variety of alteration histories that became juxtaposed through brecciation.

### 3.2. Bulk chemistry

#### *3.2.1. Major element bulk chemistry*

A CI-chondrite-normalized diagram for average bulk AOAs from Efremovka, Leoville, and Vigarano shows a tendency for progressive enrichment in more refractory elements (Fig. 3a). An exception is that the abundances of the volatile elements Na and Cl are significantly elevated in Vigarano AOAs (Fig. 3a), the obvious result of greater

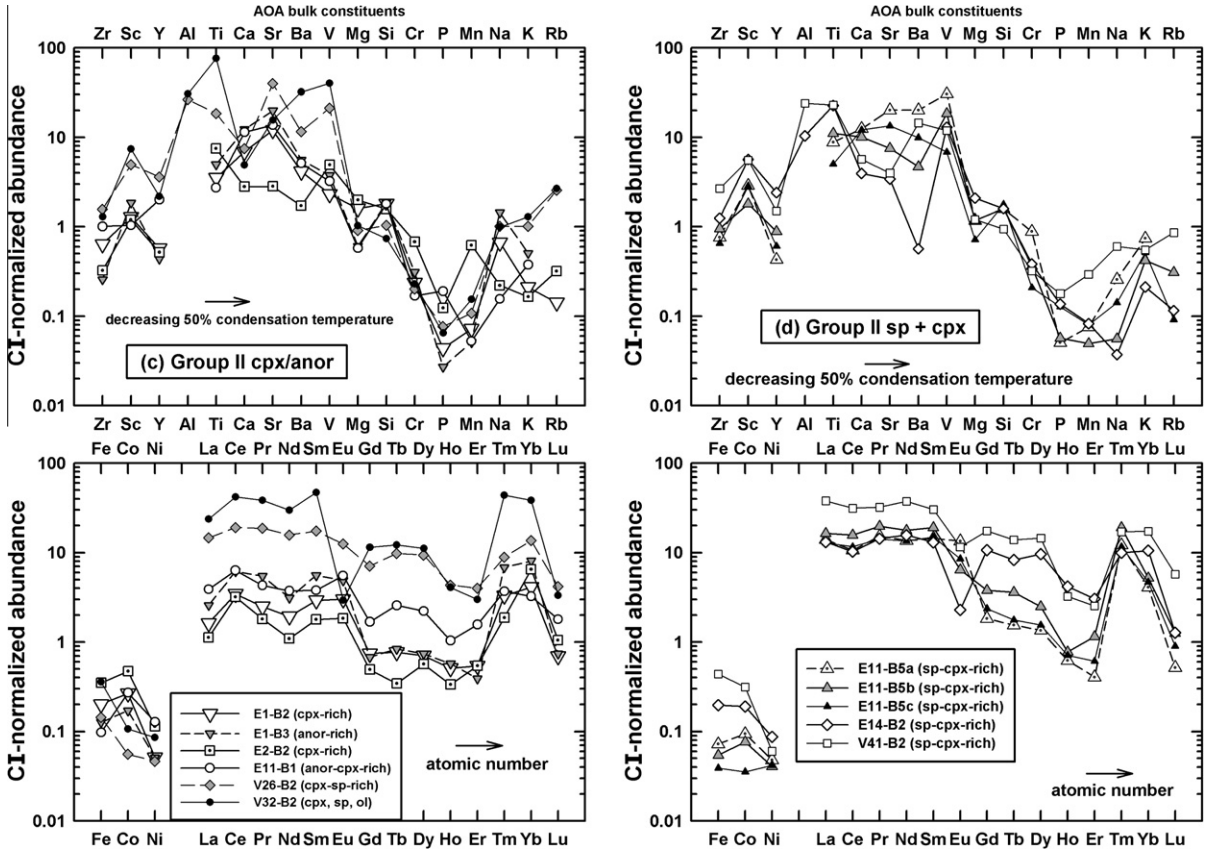


Fig. 4. *(continued)*

secondary mineralization (feldspathoid formation) experienced by inclusions from that meteorite (Section 3.1). Compared to bulk AOAs, cpx + anor-rich areas and especially spinel-rich nodules and melilite-rich areas in AOAs show greater tendency to be enriched in refractory elements (Fig. 3b).

Composite inclusions Ef-11 and Leo-29, which contain fine-grained CAIs attached to AOAs, illustrate the range of chemical variation found in inclusions and the chemical relationship between CAI and AOA material. The AOA portions of both inclusions are especially olivine-rich (Table 2). They show a similar lithophile element abundance pattern, which can be characterized as having an abundance maximum for Mg, lower abundances for more refractory elements (Al and Ca), and progressively lower abundances for increasingly volatile elements (Si through Na and Cl) (Fig. 3c–d). Thus, these olivine-rich AOAs are most enriched in elements of intermediate volatility. In contrast, the CAI and cpx + anor rich portions of the composite inclusions show a stronger pattern of refractory element enrichment (Fig. 3c–d). A notable feature is the chemical similarity between the sp + cpx and cpx + anor facies in Ef-11 (Fig. 3c).

### 3.2.2. Trace element bulk chemistry

Fig. 4 presents CI-normalized SIMS broad beam data for a variety of assemblages in AOAs. In general these data represent analyses of "bulk constituents" that include multiple minerals in the analysis volume. However, for broad beam analyses of olivine, the SIMS beam was allowed to overlap multiple adjacent olivine grains, and good agreement between broad and narrow beam data for olivine (Fig. 4a) implies that the broad beam data for it largely represent the single mineral.

For olivine, the abundances of refractory lithophile elements (Zr–Ba, REE) are relatively uniform at ~0.2–0.4 × CI chondrites, and the most volatile elements (including P, Na, K, Rb, excepting Mn) are the most depleted at ~0.02–0.1 × CI chondrites (Fig. 4a). There is an abundance maximum for elements of intermediate volatility (Mg and Si, secondarily V and Cr) (Fig. 4a). This is the same pattern as observed with DB-EMPA of olivine-rich areas (Section 3.2.1), but the many additional elements analyzed by SIMS make the relationship to volatility more obvious.

For cpx + anor regions, two types of trace element patterns were found. Twenty-two of 26 regions show the "common signature" in which refractory lithophile elements (Zr–V, REE) are relatively enriched (~5–10 × CI) compared to more volatile elements (Fig. 4b). The four remaining cpx + anor regions show Group II signatures (e.g., Davis and Grossman, 1979; Mason and Taylor, 1982; Boynton, 1985) (represented in Fig. 4c by analyses E1-B2, E1-B3, E2-B2, and E11-B1). In general, for Group II patterns there is an abundance maxima for elements of intermediate volatility (e.g., Al-V, LREE, ~2–10 × CI) relative to more refractory and volatile elements (Boynton, 1985).

In AOAs, there is no obvious textural or mineralogical distinction between cpx + anor areas that show the Group

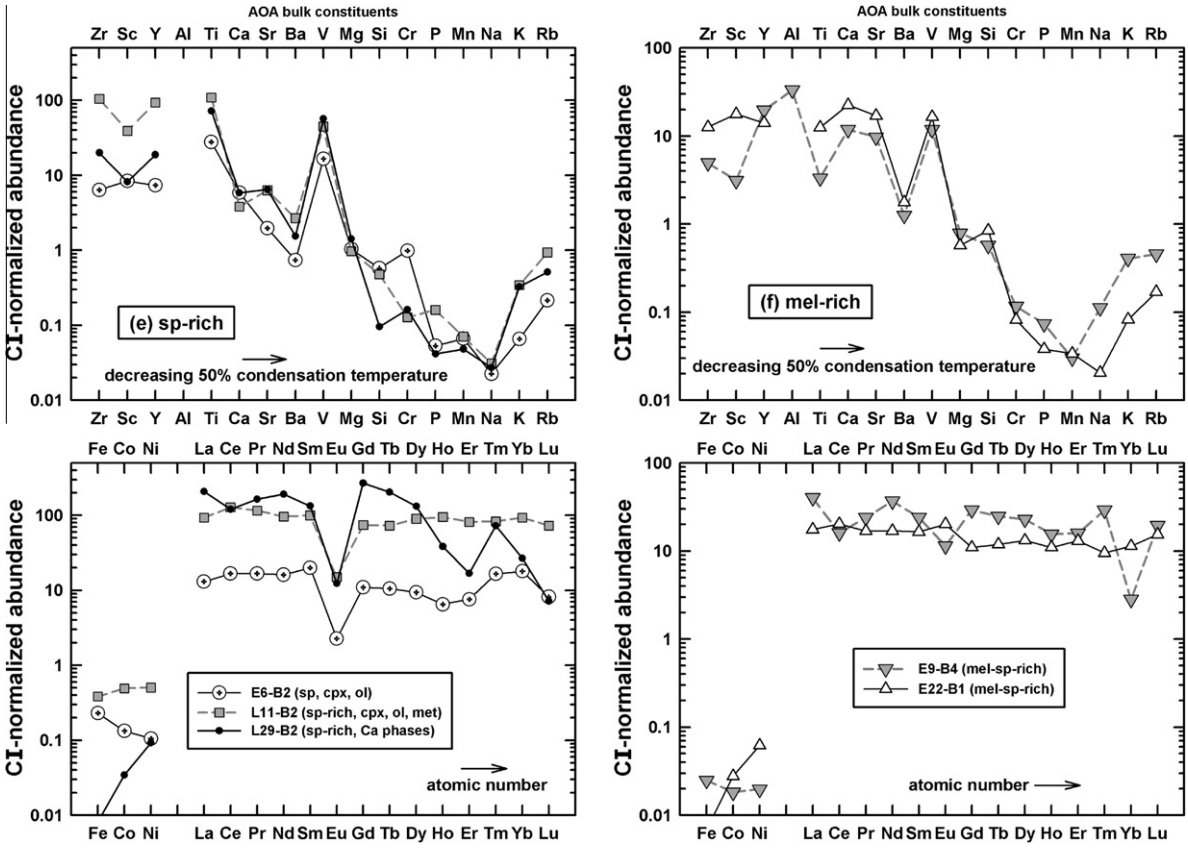


Fig. 4. *(continued)*

II signature and those that show the common signature. Moreover, similar Group II patterns occur in areas that contain variable amounts of clinopyroxene and anorthite, although Sr abundances appear to be higher in areas containing more anorthite, and V abundances appear to be higher in areas containing more clinopyroxene. In inclusions Ef-2 and Ef-11, both the common and Group II signatures were found in different cpx + anor regions, so the presence or absence of a particular trace element signature is not inclusion-specific. However, in Ef-11 there is a distinction in trace element type for cpx + anor according to facies, with the common pattern associated with the olivine-rich AOA and the Group II pattern associated with the cpx + anor facies (Fig. 1k).

Group II signatures similar to those in cpx + anor areas were observed for clinopyroxene-rich, anorthite-poor areas that contain some spinel, represented by analyses V26-B2 and V32-B2 (Fig. 4c). However, for these regions the abundances of REEs and other elements (Ti, Ba, V) are notably higher, up to 40–90 × CI, than for cpx + anor areas that contain little spinel. In addition, V32-B2 exhibits a strong negative Eu anomaly.

A variety of trace element signatures were observed for spinel-rich regions in inclusions, but all indicate enrichment in refractory elements (Fig. 4d). Areas rich in spinel + clinopyroxene, including the CAI portion of composite inclusion Ef-11, and spinel-cored nodules surrounded by clinopyroxene layers in AOAs from Ef-14 and Vig-41, show Group II patterns. The Group II patterns differ between inclusions. In Ef-11, a relatively consistent REE pattern with no Eu anomaly is observed for areas that contain variable amounts of spinel and clinopyroxene. In Ef-14 and Vig-41, negative Eu anomalies are observed.

Group II sp + cpx and cpx + anor areas have similar REE patterns, but LREE abundances are ~3–10× higher in the former (Fig. 4c–d). This bears on the possible genetic relationship between these assemblages (Section 4.1).

Spinel-rich nodules show a variety of trace element patterns (Fig. 4e). All have positive V anomalies that probably reflect an affinity for this element in the spinel structure, and all have higher relative abundances of the most refractory elements than one normally sees for Group II patterns. For example, analysis E6-B2, corresponding to a spinel-cored nodule surrounded by clinopyroxene in AOA Ef-6, shows a muted Group II pattern that does not have a strong relative depletion in the most refractory elements. For analysis L11-B2, corresponding to a spinel-rich nodule containing some melilite and perovskite embedded in an AOA, there is no hint of a Group II pattern and instead refractory elements (Zr–Ti, all REE except Eu) are strongly enriched (~40–100 × CI). Finally, analysis L29-B2, centered on a spinel-rich nodule containing perovskite and surrounded by melilite in the CAI portion of Leo-29, shows evidence of a Group II signature (i.e., a fractionated REE pattern with lower abundances of Ho, Er, Lu and a positive Tm anomaly). But unlike typical Group II patterns, L29-B2

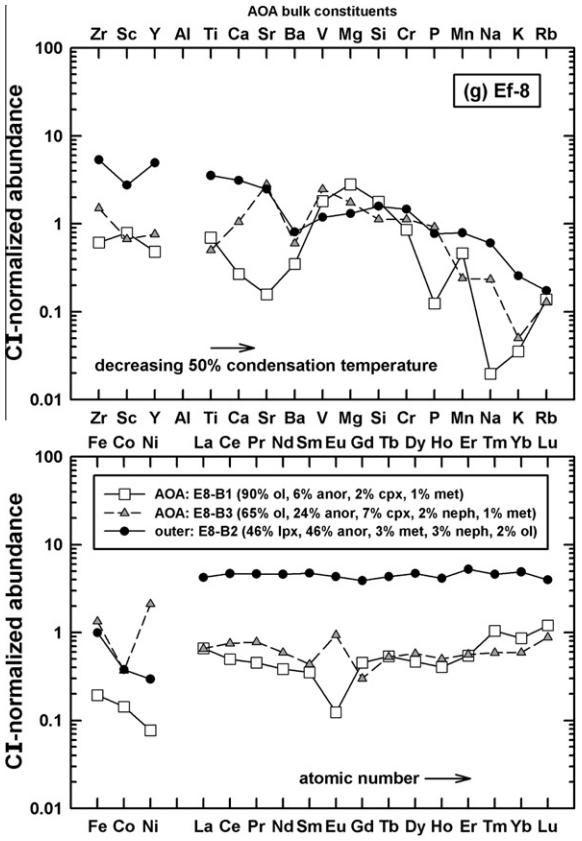


Fig. 4. *(continued)*

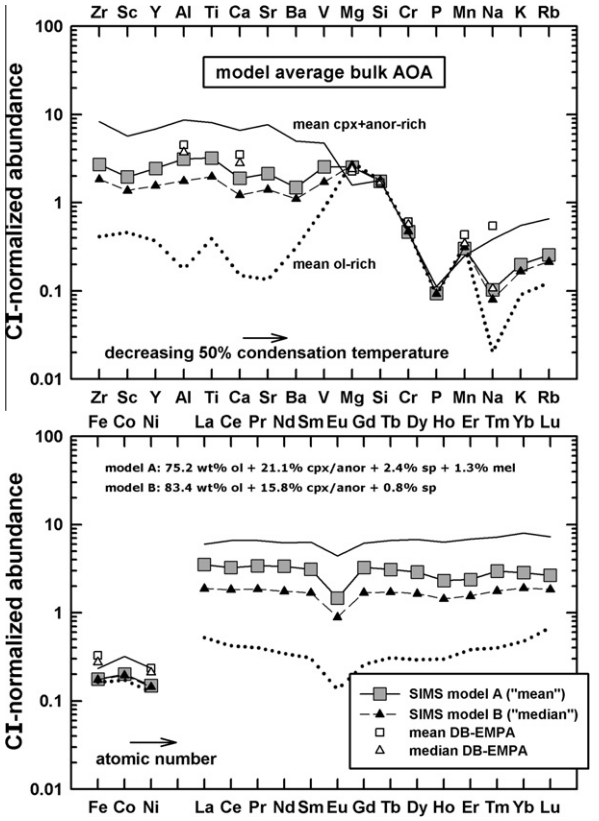


Fig. 5. CI-normalized abundances for model bulk AOAs determined by modal reconstruction utilizing SIMS data, assuming mean proportions of minerals (model A) and median proportions of minerals (model B) in AOAs. Also shown are the mean compositions for ol-rich and cpx + anor areas in AOAs, and average bulk compositions of AOAs determined by DB-EMPA. Mineral abbreviations as in Fig. 1.

has high abundances of both highly refractory elements Gd and Tb (~200–250 × CI) and less refractory LREE (~100–200 × CI).

Analyses of melilite-rich nodules in AOAs were obtained for Ef-9 and Ef-22 (Fig. 4f). Analysis E22-B1 shows a relatively uniform enrichment in refractory elements (~10–20 × CI), except for a large negative Ba anomaly. Analysis E9-B4 has a more fractionated pattern, including negative Yb, Eu, Ce, and Ba anomalies.

SIMS analyses were obtained both for the AOA core of Ef-8 as well as for the distinctive outer zone, which is rich in low-Ca pyroxene (Fig. 1h, 4g). The analysis for the outer zone (E8-B2) shows that it is enriched in refractory trace elements (average ~4.3 × CI for Zr–Ca, REE) compared to two analyses of the AOA core (E8-B1, E8-B3) (Fig. 4g). The trace element signature for E8-B2 resembles that of cpx + anor areas with the common refractory signature, except for having lower abundances of refractory elements (especially Ba, V) and no negative Eu anomaly (Fig. 4b and g).

For many of the regions analyzed by broad beam SIMS, the abundances of the alkali elements (especially K and Rb, sometimes Na) show relative enrichments compared to somewhat less volatile elements (P, Mn) (Fig. 4). This is especially true for analyses obtained for Vigarano, which has inclusions that were more affected by secondary mineralization involving replacement of anorthite by feldspathoid. As one might expect, secondary enrichment of alkalis was often important for regions rich in anorthite (Fig. 4b–c), but these effects are also seen in spinel- and melilite-rich areas (Fig. 4d–f) and even in olivine-rich areas (Fig. 4a).

Fig. 5 shows calculated average bulk compositions for AOAs by combining the mean compositions of AOA components (olivine, cpx + anor areas, spinel-rich nodules, and melilite-rich nodules) with their average proportions in AOAs. The mean olivine composition is taken from Table 3, whereas the mean cpx + anor composition is calculated as the mean of all analyses of cpx + anor assemblages, including 22 analyses with the common signature (Fig. 4b) and 4 with a Group II signature (Fig. 4c). For these calculations, metal and secondary feldspathoids were neglected; all clinopyroxene and anorthite was assumed to be present in the form of cpx + anor assemblages, and all spinel and melilite was assumed to be present in the form of spinel-rich nodules and melilite-rich nodules, respectively. For the average proportions, both mean (model A) and median (model B) values were used.

The model abundances for lithophile refractory elements are relatively uniform and elevated compared to more volatile elements (Cr, P, Mn and alkalis), with refractory element

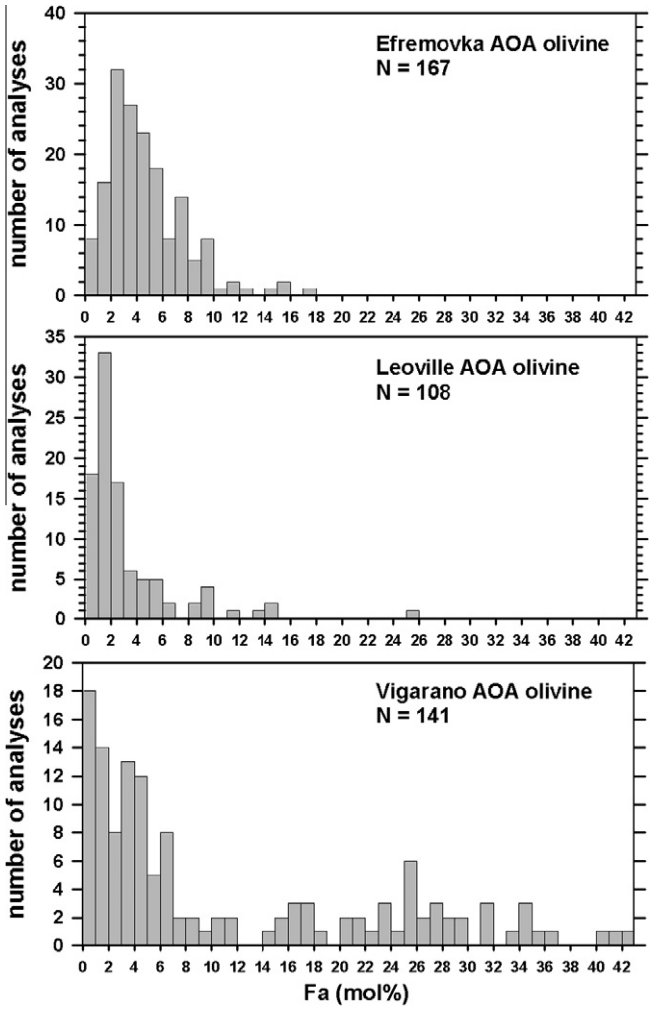


Fig. 6. Histogram of Fa values for superior EMP analyses of olivine in Efremovka, Leoville, and Vigarano. $N$ = number of analyses.

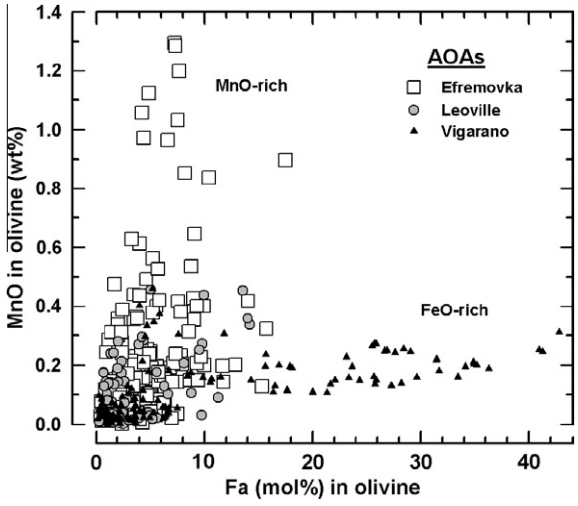


Fig. 7. Fa-MnO variation diagram for AOA olivine showing FeO-rich and MnO-rich populations in addition to the more common low-FeO, low-MnO population.

(Zr–V, REE) abundances ~2–3 × CI chondrites (Fig. 5). This is slightly lower than the average ~3–4 × CI for Al and Ca based on DB-EMPA (but within the scatter of the latter – Fig. 3a). Model abundances of ~2–4 × CI chondrites for refractory lithophile elements agree with the Group IV trace element signature typically found for olivine-rich aggregates (Mason and Taylor, 1982; Kornacki and Wood, 1984), suggesting that this is a representative bulk AOA composition. Higher abundances (up to ~10 × CI) reported for some AOAs (Grossman et al., 1979; Russell et al., 2003) likely reflect oversampling of CAI or cpx + anor materials and are not representative of typical AOAs.

### 3.3. Mineral chemistry

#### *3.3.1. Major element mineral chemistry*

Large variations in major-element composition were found for most AOA minerals with EMPA. Ranges are as follows: olivine ($Fa_{0.15–42.8}$, but mostly ~$Fa_{0–10}$), Al-diopside (0.60–27.2 wt.% $Al_2O_3$, 0.01–1.96 wt.% $TiO_2$), "fassaite" (9.9–34.7 wt.% $Al_2O_3$, 2.1–11.5 wt.% $TiO_2$), low-Ca pyroxene ($Wo_{0.76–4.7}$ $En_{88.2–97.4}$, $Fs_{1.6–7.1}$,

0.41–2.74 wt.% $Al_2O_3$), spinel (Al/[Al + Cr] = 0.99–1.00 at., Mg/[Mg + Fe] = 0.86–1.00 but mostly 0.98–1.00 at.), melilite ($Geh_{63.0–95.2}$), and anorthite ($An_{94.5–99.6}$ but mostly $An_{98–99.6}$).

The most extensive data set (397 analyses) was obtained for olivine. Histograms of fayalite contents in olivine for the three meteorites show peaked distributions at low fayalite values for each meteorite: mostly $Fa_{2–6}$ for Efremovka, mostly $Fa_{0–3}$ for Leoville, and mostly $Fa_{0–7}$ for Vigarano (Fig. 6). These distributions are similar to those reported previously for AOAs from these meteorites (Komatsu et al., 2001), except that our samples of Vigarano contain many inclusions with relatively ferrous olivine ($Fa_{10–43}$). Olivine grains within a given inclusion in Efremovka and Leoville commonly show variation of a few mol% Fa within a small area, both within and between grains. In Vigarano, larger variations in Fa values (~30 mol%) are sometimes found, with ferrous olivine occurring both in narrow rim zones of individual grains, and over larger regions (Fig. 1d). The most ferrous olivine grains in Vigarano occur in those inclusions that also contain significant feldspathoids.

Fig. 7 shows a Fa–MnO diagram for olivine. Most olivine (~80% of the analyzed grains) from the three meteorites has both low Fa values (<10 mol%) and low MnO contents (<0.5 wt.%), but some olivine in Efremovka is MnO-rich (up to 1.3 wt.%), and a significant proportion of olivine (especially from Vigarano) is FeO-rich (Fa > 10 mol%). An apparent hiatus in MnO contents occurs at ~0.7 wt.% MnO, and all but one analysis above this hiatus comes from a single inclusion, Ef-15. A large number of Mn-rich olivine grains in Ef-15 cause this inclusion to have high bulk MnO content (Table 2). Many but not all of the Mn-rich olivine grains in Ef-15 occur as shells around metal. In other inclusions, olivine grains with elevated Mn contents (higher than elsewhere in the inclusions) also tend to occur in shells around metal. However, shell olivine does not always have elevated Mn contents.

Microprobe data for olivine are summarized in Table 4, which divides olivine into four populations that mostly have low (<0.7 wt.%) MnO contents: (a) forsterite ($Fa_{1–10}$), (b) magnesian olivine (Fa 1–10), (c) ferrous olivine (Fa > 10), and (c) Mn-rich olivine (>0.7 wt.% MnO). Table 4 indicates that minor element compositions are similar in forsteritic, magnesian, and ferrous olivine, except that ferrous olivine can have an elevated Na content, and except that forsterite tends to be poorer in Mn, Ni, and Al. Fayalite values for the magnesian olivine population ($Fa_{1–10}$, mean $Fa_{3.9}$) and Mn-rich olivine population (range $Fa_{4-18}$, mainly ~$Fa_{4–10}$) overlap, but tend to be higher in the Mn-rich grains.

The Mn-rich olivine in Efremovka somewhat resembles Mn-rich forsterites ("LIME"—low iron, manganese enriched) found in IDPs, chondrite matrices, and AOAs from CR chondrites (Klöck et al., 1989; Weisberg et al., 1993, 2004) except that it is more ferrous. Mn-rich fayalites from chondrites are also known (e.g., Krot et al., 2000b; Zolotov et al., 2006), but the Efremovka grains are far less iron rich. The Efremovka grains most closely chemically resemble Mn-rich olivine found recently in samples of comet nucleus 81P/Wild 2 (Zolensky et al., 2006; Nakamura et al., 2008).

### 3.3.2. Trace element mineral chemistry

Ion probe narrow beam data for minerals are given in Table 5 and are shown as CI-normalized abundances in Fig. 8. Analyses were obtained for relatively pure olivine, Al-diopside, fassaite, low-Ca pyroxene, melilite, and spinel, although owing to fine grain size only limited data are available for phases other than olivine.

Narrow beam analyses for olivine (Fig. 8a) yield compositions similar to broad-beam analyses for olivine-rich areas in AOAs. Analysis E2-2 from Ef-2 is an example of "shell"

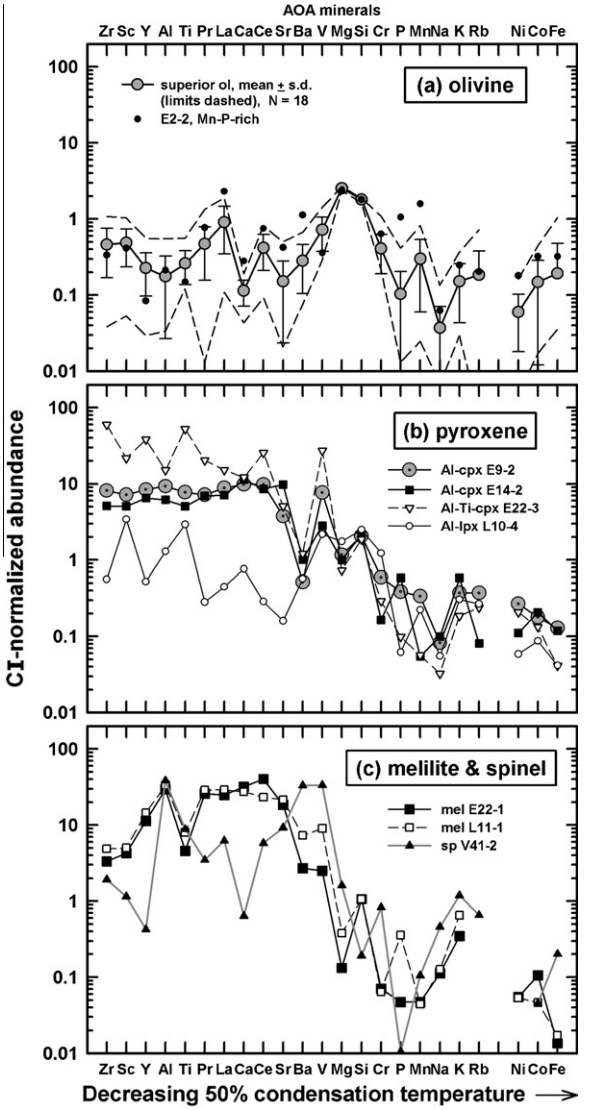


Fig. 8. CI-normalized abundances determined by narrow beam SIMS. (a) Olivine. Points show mean values, bars standard deviations, and dashes compositional extremes for 18 analyses excluding Mn-rich E2-2 (shown separately). (b) Pyroxene, including Al-diopside (analyses E9-2, E14-2), fassaite (E22-3), and aluminous low-Ca pyroxene (L10-4). (c) Melilite (analyses E22-1, L11-1) and spinel (V41-2).

olivine around metal that is significantly richer in MnO (0.41 wt.%) than other grains analyzed by SIMS (mean 0.08 wt.%). Besides high Mn, this grain also contains roughly ~10× more phosphorus than average AOA olivine (Fig. 8a, Table 5). E2-2 also has elevated contents of La, Ca, Ba, Ni (the latter possibly caused by proximity to metal) and a lower content of V than other analyzed olivine (Fig. 8a).

Analyses of pyroxene are shown in Fig. 8b. Two analyses of Al-diopside have abundances that are generally similar to cpx + anor areas with the common signature, except that Al-diopside has much lower abundances for Ba and Sr. This observation implies that in cpx + anor areas, the latter two elements are concentrated in anorthite and most other elements are concentrated in Ca-pyroxene. Compared to Al-diopside, "fassaite" (technically a solid solution of grossmanite, kushiroite and diopside as defined by Ma and Rossman (2009) and Ma et al. (2010)) is more enriched in refractory elements, especially Ti, V and the highly refractory elements Zr, Sc and Y (Fig. 8b). The composition of this fassaite is generally similar to that of a spinel-rich nodule in Leo-11 (analysis L11-B2, Fig. 4e), although it is less refractory. A single analysis of low-Ca pyroxene from the poikilitic (possibly melted) periphery of Leo-10 shows a relatively fractionated pattern, with no obvious correlation with condensation temperature (Fig. 8b). This low-Ca pyroxene has relatively high abundances of elements with intermediate volatility (V, Mg, Si, Cr) and also low volatility (Sc, Ti).

Two analyses of melilite are shown in Fig. 8c. These analyses, E22-1 from Ef-22 and L11-1 from Leo-11, indicate that the melilite is enriched in refractory elements, especially Al, La, Ce, Pr, Ca and Zr, and that it has lower abundances of more highly refractory elements (Zr, Sc and Y) (Fig. 8c). This suggests a Group II signature for the melilite. However, broad beam analysis of a separate melilite-rich nodule in Ef-22 (E22-B1, Fig. 4f) shows only a hint of a Group II signature. Moreover, analysis of a separate melilite-bearing, spinel-rich nodule in Leo-11 (L11-B2, Fig. 4e) shows no evidence for a Group II pattern. Thus, different melilite-bearing areas in the same inclusions can have different trace element patterns, both Group II and non-Group II refractory, like cpx + anor areas.

A single analysis of spinel shows a highly fractionated trace element pattern (Fig. 8c). The spinel is generally enriched in refractory elements (elements more refractory than Si), especially Al, Ba, and V, but has much lower abundances of Y and Ca.

## 4. DISCUSSION

### 4.1. Trace element evidence for a condensate origin for AOAs

Trace element data provide strong evidence that AOAs are condensates. Specifically, the data imply that some AOA components originated by fractional condensation or fractional vaporization, that some AOA assemblages represent condensates that reacted with a surrounding (likely gaseous) medium, and that some components in AOAs are vaporization residues.

#### *4.1.1. Fractional condensation/vaporization*

Good evidence for condensation is provided by the presence of Group II trace element patterns for some spinel-rich and cpx + anor assemblages (Fig. 4c–d). Group II patterns are uniquely explained by condensation of a gas from which a more refractory condensate was previously removed (e.g., Boynton, 1975; Davis and Grossman, 1979). It appears that there are only two options for creating the Group II signatures in AOAs. Either they formed by fractional condensation as temperature decreased monotonically, or they formed as condensates from a gas that was generated after isolation of a residue following partial vaporization/sublimation ("fractional vaporization").

Olivine in AOAs shows no chemical evidence for melting processes. The abundance pattern for olivine (Fig. 4a) lacks an enrichment of HREE relative to LREE, and lacks an enrichment of weakly incompatible Sc relative to highly incompatible Zr, features that one might expect for igneous partitioning.

Instead, the composition of AOA olivine is more consistent with condensation following the removal of a refractory component, either by fractional condensation or by condensation following fractional vaporization, resulting in abundance maxima for elements of intermediate volatility (Mg, Si, V, Cr). This is analogous to producing refractory condensates with a Group II signature, but with fractionation occurring at a lower temperature.

The olivine in AOAs shows a complementary composition to cpx + anor assemblages, the prevalent refractory material in AOAs. That is, relative to Si (which has similar abundance in both olivine and cpx + anor), the common cpx + anor areas are uniformly enriched in refractory elements and depleted in Mg, whereas the olivine is uniformly depleted in refractory elements and enriched in Mg (Fig. 5a–b). Thus, partial segregation of a refractory condensate similar in composition to cpx + anor (or its CAI precursor—Section 4.1.2) could have resulted in a gas out of which the olivine condensed.

We interpret the AOA model composition (Fig. 5) as indicating that an average AOA formed as a condensate at an elevated temperature in a closed system that had roughly chondritic bulk composition. Owing to elevated temperature, elements more volatile than Si were substantially present in a gas phase. Given that AOAs are composed of both refractory (Al-rich) and less refractory (olivine) materials with significantly different compositions, the uniform enrichment in refractory elements suggests that the more and less refractory materials in them are complementary and genetically related. Otherwise one would not expect chondritic ratios for so many refractory elements.

#### *4.1.2. Reaction of condensates with a gas*

We infer that cpx + anor regions in AOAs represent CAI assemblages that partially reacted with a surrounding gaseous medium. Two types of trace element patterns (Group II and common refractory) are observed for cpx + anor assemblages, and we infer that two types of CAI precursors were present.

Assemblages of cpx + anor with Group II patterns probably formed by transformation of fine-grained

sp + cpx CAI assemblages that had Group II patterns. Sp + cpx and cpx + anor regions have similar compositions, as illustrated by major element compositions in composite inclusion Ef-11 (Fig. 3c), and by Group II trace element signatures for sp + cpx and some cpx + anor regions (Fig. 4c–d). The main chemical difference between the two assemblages is that the abundances of the most refractory elements are higher in areas that contain more spinel. This suggests that sp + cpx assemblages could have been transformed to cpx + anor assemblages by the loss of refractory elements, or by the dilution of refractory elements after volatile element addition from a gas phase.

Similarly, patches of cpx + anor in AOAs with the common refractory trace element signature (Fig. 4b) were probably formed by transformation of CAI-like material that was uniformly enriched in refractory elements. Analyses of suitable CAI precursor material include analysis E22-B1 of a melilite-rich nodule in Ef-22 (Fig. 4e), and analysis L11-B2 of a melilite-bearing spinel-rich nodule in Leo-11 (Fig. 4e). Both contain a significant melilite component; both are enriched in refractory elements but do not show a strong Group II signature; and both have lower abundances of Mg and Si and higher abundances of REE and most other refractory elements compared to cpx + anor areas. This supports the idea that melilite-bearing assemblages were converted into cpx + anor patches by the addition of Mg and Si from a gas phase (Krot et al., 2004a,b,c). Based on the prevalence of cpx + anor areas with the common refractory pattern, it appears that melilite-bearing assemblages with uniform enrichments of refractory abundances could have been relatively common in AOAs.

*4.1.3. Vaporization residues*

We infer that vaporization played a role in producing some Al-rich AOA components to result in distinctive trace element compositions. For example, analysis L29-B2 of a spinel-rich nodule appears to show a modified Group II pattern, with HREE abundances higher than one normally sees, and very high abundances of some REE (up to ~100–300 × CI) (Fig. 4e). We suggest this nodule represents a vaporization residue of an original Group II condensate, with the composition reflecting both condensation (the quasi-Group II-like pattern) and vaporization (the elevated abundances of REE and especially of Gd and Tb). Analysis L11-B2 of a spinel-rich nodule has relatively high abundances (~70–100 × CI) of highly refractory elements (Zr, Sc, Y, Ti, most REE) with a highly prominent negative Eu anomaly (Fig. 4e). Europium is the most volatile REE under most conditions (Boynton, 1975, 1978; Boynton and Cunningham, 1981), so both the Eu anomaly and high abundances of refractory trace elements are consistent with this nodule being a vaporization residue. Analysis E9-B4 of a melilite–spinel ribbon in Ef-9 (Fig. 4f) has an irregular REE pattern but with negative anomalies in three elements that can be relatively volatile under different redox conditions (i.e., Yb and Eu are volatile under reducing conditions, and Ce and Eu are volatile under oxidizing conditions—Boynton, 1978; Davis et al., 1982). This ribbon could have experienced multiple heating events under different redox conditions.

Given the variety of patterns, it is clear that these Al-rich nodules and ribbons could not all have formed under the same conditions from the same starting materials. The lack of a simple "super-refractory" pattern also implies that the

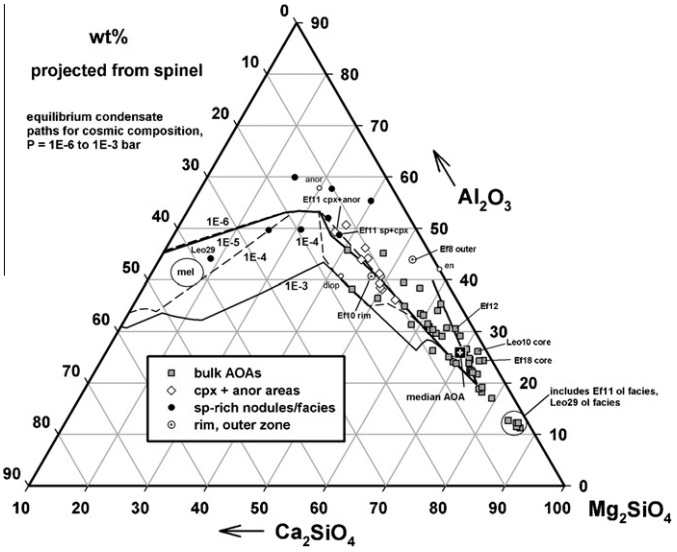


Fig. 9. The bulk compositions of AOAs and some of their constituents based on DB-EMPA are projected from spinel ($MgAl_2O_4$) on a corundum ($Al_2O_3$) – larnite ($Ca_2SiO_4$) – forsterite ($Mg_2SiO_4$) ternary (projection after Huss et al., 2001). For reference, small open symbols show the compositions of pure minerals (en = enstatite, anor = anorthite, diop = diopside). Lines show predicted compositions of equilibrium condensates at four different pressures ($10^{-6}$, $10^{-5}$, $10^{-4}$, and $10^{-3}$ bar) for a cosmic (solar) composition at a range of temperatures (higher temperatures to left, with all paths converging at low temperatures to solar composition close to enstatite). Compositions of cpx + anor regions (including Ef-10 rim protrusion) and some bulk AOAs appear to more closely match condensates predicted for low pressures ($10^{-6}$ and $10^{-5}$ bar) than for high pressures ($10^{-4}$ and $10^{-3}$ bar).

compositions of these materials reflect multiple events and disequilibrium.

### 4.2. Major element evidence for a condensate origin for AOAs

Strong evidence for a condensate origin of AOAs is provided by comparing the major-element chemical trends for bulk AOAs and their components with predicted trends assuming equilibrium in a system of approximately solar composition. Data-model comparisons are given in Fig. 9–11 for different plausible nebular pressures ($10^{-3}$–$10^{-6}$ bar).

Figs. 9 and 10 show comparisons for two ternary projections involving Mg, Si, Ca, and Al. The composition of bulk AOAs and cpx + anor areas lie close to the predicted condensate trends, with cpx + anor areas and bulk AOAs corresponding to higher temperature and lower temperature, respectively (Figs. 9 and 10). This is consistent with higher abundances of refractory elements in cpx + anor assemblages (Fig. 5).

The overall composition of low-Ca-pyroxene-bearing inclusion Ef-12 (Fig. 1g) lies close to a low-temperature segment of the predicted condensate trend (Fig. 9). This suggests formation of Ef-12 as a relatively low temperature condensate. The inclusion is relatively porous and the low-Ca pyroxene within it is concentrated near the inclusion periphery, features consistent with the formation of low-Ca pyroxene by condensation/reaction processes involving Si addition (Krot et al., 2004a,b, 2005).

There are two types of notable deviations evident between observed and equilibrium compositions in Figs. 9 and 10. The compositions of spinel-rich nodules lie off the predicted equilibrium compositions towards spinel (Fig. 10), and the bulk compositions of some olivine-rich AOAs lie off the predicted equilibrium paths towards forsterite (Figs. 9 and 10). We suggest that both of these discrepancies reflect disequilibrium, but in somewhat different ways.

Spinel-rich material could have formed rapidly and under disequilibrium, either as a vaporization residue or as a condensate. As noted above (Sec. 4.1), there is trace-element evidence for both of these processes operating to various extents in different spinel-rich materials. The silicate portions of spinel-rich nodules lie close to predicted condensate compositions (Fig. 9), suggesting that the overall discrepancy with predicted condensate compositions is caused by an excess of spinel.

Examples of AOAs that have major-element compositions which extend past the predicted condensate trend to more olivine-rich compositions include the olivine-rich facies (AOA portions) of composite inclusions Leo-29 and Ef-11 (Fig. 1k and l). These AOAs are attached to CAIs and have an apparent overabundance of olivine relative to equilibrium condensates (Fig. 9). The discrepant compositions for these inclusions could be explained as an artifact of non-representative sampling of olivine and Al-rich components in two-dimensional sections, and although this is plausible for small inclusions, it seems unlikely for a large inclusion such as Ef-11. Instead, we suggest that these olivine-rich compositions resulted from condensation following the removal of a higher temperature component under disequilibrium conditions. For example, removal of an Ef-11-like sp + cpx CAI condensate from anywhere along the main AOA trend would have driven the remaining gas composition towards forsterite in Figs. 9 and 10, from which olivine in Al-Ca-poor AOAs such as Ef-11 and Leo-29 could condense.

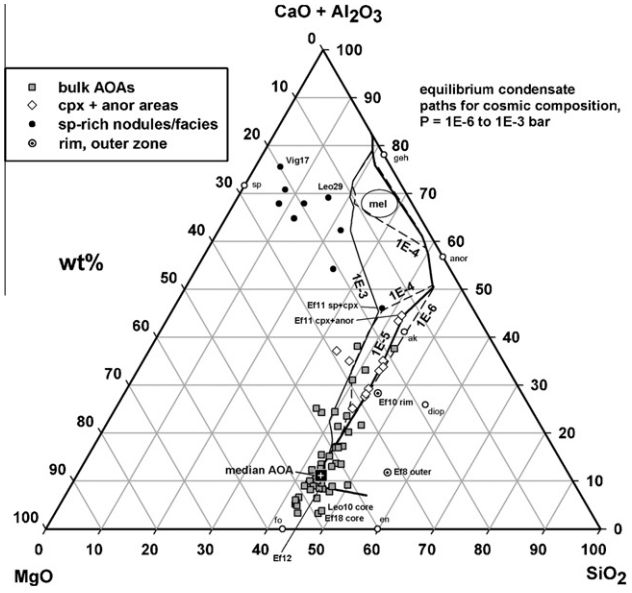


Fig. 10. Bulk compositions of AOAs and some of their constituents based on DB-EMPA are projected on an MgO – SiO2 – CaO + $Al_2O_3$ ternary. Graphic elements and notations are the same as in Fig. 1 and Fig. 9; also fo = forsterite, ak = akermanite, geh = gehlenite. The compositions of sp-rich nodules are displaced off of predicted condensate compositions towards spinel, but more closely approach those predicted for condensates produced at high pressure ($10^{-3}$ bar) than at lower pressure.

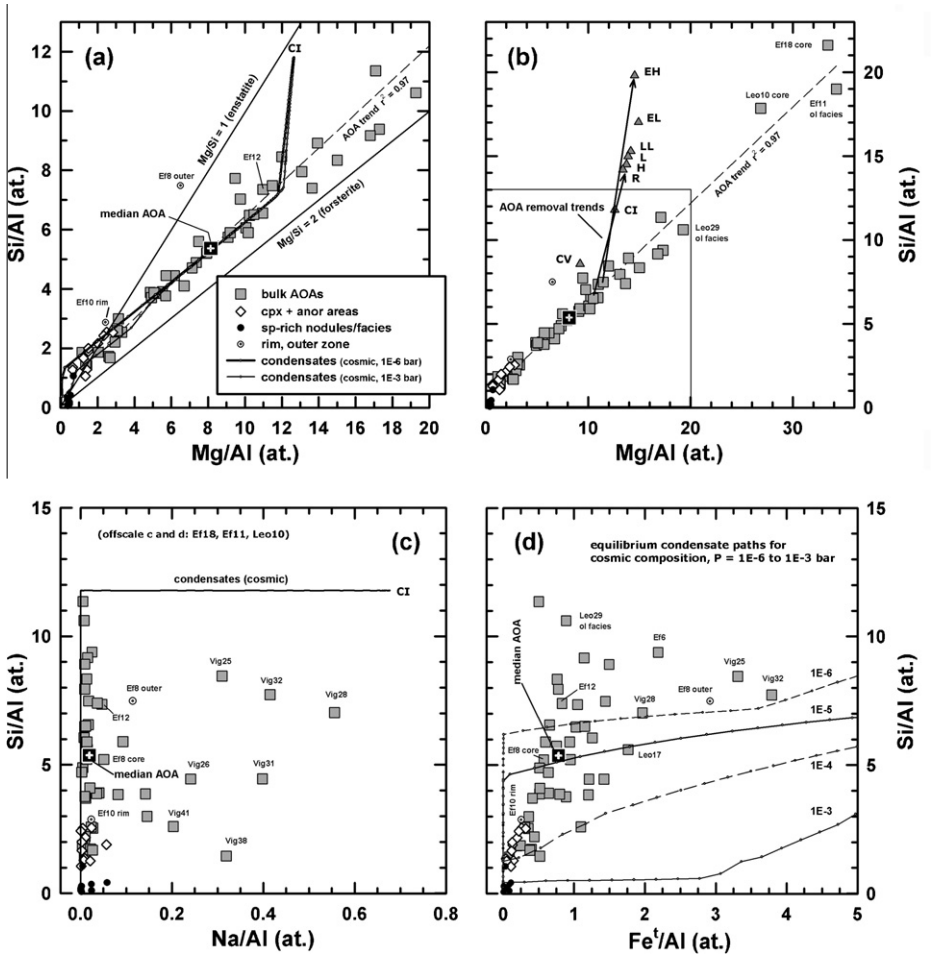


Fig. 11. The bulk compositions of AOAs and some of their constituents based on DB-EMPA are shown in Al-normalized variation diagrams. Data are compared to predicted compositions of equilibrium condensates at various pressures in a system of cosmic composition at a range of temperatures; higher-temperature assemblages (more refractory compositions) lie closer to the origin in all diagrams. (a) Si/Al vs. Mg/Al diagram, showing that the compositions of most AOAs and cpx + anor areas resemble those predicted for equilibrium condensates. (b) Si/Al vs. Mg/Al diagram showing the complete range of data for AOAs; tie lines (AOA removal trends) can be drawn between points on the AOA and condensate trends near Mg/Al ~11 and Si/Al ~7 through the CI chondrite composition to the average compositions of R, H, L, LL, EL, EH chondrites (data from Wasson and Kallemeyn, 1988; Jarosewich, 1990; Hutchison, 2004); the implications of this are discussed by Ruzicka et al. (2011). (c) Si/Al vs. Na/Al diagram showing that some Vigarano inclusions have notably high Na/Al caused by secondary feldspathoid formation and that most others have compositions which resemble those of predicted condensates. (d) Si/Al vs. $Fe^t$/Al ($Fe^t$ = total Fe) diagram, showing that Si/Al and $Fe^t$/Al are generally correlated for AOAs and cpx + anor areas, but that the pattern of variation does not closely match that predicted for equilibrium condensates at a single pressure.

Other useful comparisons can be made by utilizing Si/Al vs. Mg/Al, Na/Al and $Fe^t$/Al ($Fe^t$ = Fe total) plots (Fig. 11). Such diagrams emphasize the proportion of refractory (Al-rich) material to less refractory material.

In terms of Si/Al vs. Mg/Al, all bulk AOAs fall on a single well-defined AOA trend, and cpx + anor areas lie close to this trend at the high Al end (Fig. 11a–b) (Most spinel-rich areas lie off the trend.). The AOA trend substantially overlaps predicted condensate compositions (Fig. 11a–b). The composition of predicted equilibrium condensates deviate to lower Mg/Si values at lower temperatures, reflecting an increase in the low-Ca pyroxene/olivine ratio as low-Ca pyroxene becomes more stable (Fig. 11a). The bulk compositions of AOAs do not show evidence for such systematic addition of low-Ca pyroxene. Furthermore, the Al-deficient compositions shown by some AOAs cannot be explained by equilibrium condensation, as noted above. Instead, the large compositional spread for AOAs in terms of Si/Al and Mg/Al values along a single trend is best explained by variable sampling of olivine-rich and cpx + anor materials. These materials likely originated as condensates at different temperatures, but largely above the temperature at which low-Ca pyroxene was stable.

The "refractory element fractionation" experienced by non-C chondrites (Larimer and Anders, 1970; Larimer, 1979; Kerridge, 1979; Hutchison, 2004) can be explained by removal of an AOA component (Larimer and Wasson, 1988) that is olivine-rich with a relatively dilute proportion

of Al-rich material (Ruzicka et al., 2011; Fig. 11b). This could be an average AOA composition in the source regions of non-C chondrites.

In a plot of Si/Al vs. Na/Al, most AOAs have bulk compositions that lie close to the predicted condensate trend at low Na/Al, whereas others show large deviations to higher Na/Al (Fig. 11c). Those inclusions with the highest Na/Al values are all from Vigarano, and clearly were affected by secondary influx of Na during alteration.

Bulk AOAs and cpx + anor areas in AOAs show an overall co-variation in Si/Al vs. $Fe^t$/Al values (Fig. 11d). Although this is qualitatively similar to what one would expect based on volatility (Si and Fe are relatively volatile compared to Al), in detail there is poor agreement between the observed pattern of co-variation and the predicted condensate trends (Fig. 11d). $Fe^t$/Al values are approximately zero but increase rapidly at lower temperatures relative to Si/Al when metal begins to condense, unlike the pattern for AOAs (Fig. 11d). Some of the observed scatter of AOA compositions to higher $Fe^t$/Al values is caused by high FeO associated with secondary mineralization (as in Vig-32, Vig-25, Vig-28, Leo-17). Other inclusions with relatively high $Fe^t$/Al and Si/Al values are enriched in olivine (e.g., Leo-29 olivine facies) or enriched in both olivine and metal (e.g., Ef-6).

The best explanation for the overall Si/Al vs. $Fe^t$/Al trend for AOAs (excluding those with high secondary FeO) is that it reflects variable sampling of Al-rich material (similar to that of cpx + anor areas) and olivine-rich condensates that contain generally low amounts of metal. The latter condensates can be produced at low pressures, e.g., $10^{-6}$ bar or less (Fig. 11d). However, it is also possible that metal became fractionated from olivine (Section 4.4), in which case bulk $Fe^t$/Al values and metal contents do not strongly constrain pressure.

### 4.3. Formation conditions for AOAs

The composition and mineral stratigraphy of AOAs (refractory nodules embedded in an olivine-metal assemblage, assemblages rich in low-Ca pyroxene present on the margins of some olivine-rich objects) resemble what one would expect for successive quasi-equilibrium assemblages during falling temperature in a low-pressure, solar composition system. We used the CWPI code (Petaev and Wood, 1998, 2005) to place constraints on AOA formation conditions by varying pressure $P$, temperature $T$, and system composition. As explained below, we infer that AOAs formed in a system of near-canonical solar composition (with "dust/gas" $D/G \sim 1$) at $T \sim 1200$–$1384$ K and $P \sim 10^{-6}$–$10^{-4}$ bar. Solar compositions appear to provide the best matches to AOAs. In general, our inferences are similar to the conclusions of Krot et al. (2004b) and Petaev and Wood (2005), who suggested $T \sim 1230$–$1350$ K and $P \sim 6 \times 10^{-6}$–$10^{-4}$ bar for AOAs using a somewhat different analysis.

AOA formation pressures are constrained both by bulk composition and stratigraphic relationships. The bulk compositions of AOAs and cpx + anor areas are well matched at low pressures ($P \sim 10^{-6}$–$10^{-5}$ bar), and less well matched at higher pressures ($P \sim 10^{-4}$–$10^{-3}$ bar) (Figs. 9 and 10). We agree with Petaev and Wood (2005) that AOAs formed at $P < 10^{-4}$ bar, based on (1) good evidence for cpx + anor forming at a higher $T$ than olivine (more refractory cpx + anor patches embedded in olivine), implying $P < 4 \times 10^{-4}$ bar, and (2) evidence that metal formed after a period of olivine-only growth (AOAs with metal-rich peripheries), implying $P < 10^{-4}$ bar. There is also good evidence in AOAs that spinel formed at a higher temperature than either olivine (implying $P > 10^{-5}$ bar) or cpx + anor (implying $P > 4 \times 10^{-5}$ bar). A seemingly narrow range of formation $P \sim 4 \times 10^{-5}$–$9 \times 10^{-5}$ bar is thus implied.

However, the actual pressure range could have been larger if AOAs formed under disequilibrium or non-isobaric conditions. The condensation temperature for spinel increases dramatically with an increase in $P$, and condensate compositions approach those for spinel-rich nodules at high $P$ ($\geqslant 10^{-3}$ bar) and $T$ (Fig. 10). Thus, spinel-rich areas may have formed at elevated $P$, and other AOA constituents at lower $P$. Given the uncertainties, we suggest that an overall $P \sim 10^{-6}$–$10^{-4}$ bar satisfies most of the constraints for AOAs and was the main pressure regime under which AOAs formed.

To constrain $T$, we consider those AOAs that have bulk Si/Al ~1–7 at., which include most of the AOAs analyzed, and which have compositions that coincide with equilibrium condensate trajectories for the relevant range of pressures (Fig. 11a). For Si/Al values close to 1, the equilibrium mineral assemblage is dominated by cpx + anor, whereas for Si/Al values increasing above 7, low-Ca pyroxene becomes an increasingly important constituent. For $P = 10^{-6}$ bar, Si/Al values of 1–7 correspond to $T \sim 1266$–$1200$ K. For $P = 10^{-4}$ bar, they correspond to ~1384–1316 K. Thus, the likely formation temperatures for AOAs were ~1200–1384 K. A minor proportion of Al-rich materials in AOAs (spinel- and melilite-bearing nodules) would have formed at a higher $T$.

Although different temperatures are implied for the range of assemblages and bulk compositions in AOAs, it should be pointed out that some of the variation in bulk compositions is almost certainly the result of non-representative sampling. There is no guarantee that two dimensional sections will provide a representative slice of a three dimensional object. Moreover, brecciation clearly affected many AOAs, and there is no guarantee that this would result in representative pieces of the original AOAs. What can be said confidently is that the different components of AOAs formed over a range in temperatures, and that AOAs as a whole represent disequilibrium assemblages.

### 4.4. Fractionation of metal from olivine in the AOA source region

As noted previously (Section 4.2), equilibrium models indicate that the metal contents of condensates increase sharply as temperature is lowered below the condensation temperature for metal. The only way to avoid a large amount of metal for olivine-rich equilibrium condensates in a system of solar composition would be for the condensates to form over an exceedingly narrow temperature

range. For a solar composition system with $P \sim 10^{-6}$–$10^{-4}$ bar, this temperature interval is only ~2–8 K, based on the spread of observed $Fe^t/Al$ values for AOAs (Fig. 11d). It seems much more likely that AOAs formed over a larger temperature range and that metal was fractionated from olivine in AOA source regions, so that the full complement of metal that was thermodynamically stable was not incorporated into AOAs.

This inference is supported by the existence of relatively metal-poor AOAs that contain low-Ca pyroxene. In a cosmic composition system low-Ca pyroxene is generally stable at lower temperatures than metal (except at $P < 10^{-7}$ bar—Petaev and Wood, 2005), so low-Ca-pyroxene-bearing equilibrium condensates should be metal-rich if all of the metal was incorporated into the condensates. For example, just below the condensation temperature of low-Ca pyroxene at 1194 K and $10^{-6}$ bar, equilibrium models predict condensates will contain 2.6 mol% low-Ca pyroxene, 51% olivine, and 40% Fe–Ni metal. Similarly, just below the condensation temperature for low-Ca pyroxene at 1302 K and $10^{-4}$ bar, models predict 1.8% low-Ca pyroxene, 36% olivine, and 58% metal. As low-Ca-pyroxene-bearing AOAs such as Ef-12 have bulk metal contents <1 vol.% (Table 2), metal incorporation into low-Ca pyroxene-bearing AOAs must have been suppressed. The same is likely true for AOAs in general, which have <2 vol.% metal on average (Table 2), although some AOAs are more metal-rich (Weisberg et al., 2008).

The question then arises as to how metal suppression occurred. We consider two possible explanations: either (1) kinetic barriers hindered metal from nucleating and growing as a condensate (equilibrium was not maintained), or (2) one or more physical differences between metal and olivine caused differential aerodynamic sorting between these minerals during aggregate growth. Of the two possibilities, we suggest that the latter was more likely. The common presence in AOAs of metal grains surrounded by olivine shells imply that olivine preferentially nucleated and grew on metal because it was energetically favorable. The lack of analogous metal shells around olivine implies that metal did not experience the same nucleation difficulty. Thus, metal was probably less difficult to condense than olivine, rather than more difficult.

A fundamental property of chondritic particles that appears to have played an important role in aerodynamic sorting is stopping time ($t_s$), the time needed for a particle placed in a moving gas to attain the same velocity as the gas (e.g., Cuzzi and Weidenschilling, 2006). As $t_s \propto (r \cdot \rho_p)$, where $r$ = particle radius and $\rho_p$ = particle internal density, larger and denser particles will have larger stopping times and will travel further before coupling to a moving gas. Metal and olivine grains in AOAs have approximately the same size but metal is twice as dense as silicates, indicating that stopping time for metal particles will be roughly twice that of olivine particles. We suggest that this difference in density resulted in differential sorting between olivine and metal, causing metal-rich condensates to accumulate elsewhere and not as AOAs. It is conceivable that the metal grains that did agglomerate into AOAs did so precisely because they were composite particles coated by olivine (Section 3.1), which would lower the overall density of the combined particle and make the stopping time more similar to that of olivine alone. Metal grains are concentrated near the edges of most AOAs, so evidently a period of olivine growth preceded the formation of metal, at which time metal and olivine formed concurrently.

### 4.5. Olivine in AOAs—secondary processing and disequilibrium

The composition of olivine grains in AOAs from Efremovka, Leoville, and Vigarano appears to reflect secondary processing and disequilibrium. Virtually all of the iron in AOA olivine with Fa >2 (or even Fa >0.7) probably reflects secondary processing of some sort (e.g., Krot et al., 2004a; Sugiura et al., 2009). Ferrous olivine in AOAs is widely recognized as having been produced by low-temperature parent body processes (dry or fluid-assisted metamorphism) (e.g., Chizmadia et al., 2002; Fagan et al., 2004; Krot et al., 2004d), and we attribute FeO-rich olivine in Vigarano AOAs (Fig. 7) to asteroidal alteration. This is supported by the common association of FeO-rich olivine with secondary feldspathoids that are most likely to have formed in the parent body.

Less clear is the origin of MnO-rich olivine (Fig. 7). MnO-rich olivine could have formed by (1) asteroidal alteration, (2) reduction from FeO-rich olivine, or (3) condensation.

Mn-rich fayalites (up to ~1.5 wt.% MnO) that likely originated by asteroidal hydrothermal alteration have been widely reported in chondrites (e.g., Krot et al., 2000b; see references summarized by Zolotov et al., 2006), and could be the consequence of aqueous solutions that had elevated activities of $Mn^{2+}$ species (Zolotov et al., 2006). However, the MnO-rich olivine found in Efremovka is not associated with petrographic evidence for alteration, and it is much less ferrous than the Mn-rich fayalites. Clearly, the MnO-rich olivine did not form under the same conditions that were responsible for forming Mn-rich fayalites or the FeO-rich olivine in Vigarano AOAs (Fig. 7).

Reduction of FeO-rich olivine to more magnesian olivine would enrich the olivine in other elements by the removal of FeO and would produce Fe-metal. This potentially could account for the association of MnO-rich olivine with metal in AOAs. However, the metal in AOAs is not especially Ni-poor (Weisberg et al., 2004), as would be expected if it formed by reduction of FeO. Moreover, there is no evidence that MnO-rich olivine is enriched in minor elements other than Mn compared to FeO-rich olivine (Table 4). Thus, the reduction mechanism is unlikely.

The other possibility is that MnO-rich olivine was produced by condensation, which equilibrium models suggest should occur by the diffusion of Mn into previously condensed olivine. A single SIMS analysis of Mn-enriched olivine revealed an anomalously high phosphorus content (Fig. 8a, Table 5). As both Mn and P are volatile elements, this suggests the possibility of a low-temperature origin for this type of olivine, potentially consistent with low-temperature condensation. Condensation has been proposed for "LIME" forsteritic olivines in IDPs and chondrite matrices

(Klöck et al., 1989) and in AOAs from CR chondrites (Weisberg et al., 2004; Ebel and Weisberg, 2011). Petaev and Wood (2005) modeled the composition of Mn-rich (up to 0.6 wt.% MnO) forsterites and concluded that these grains could have formed at relatively low temperatures (above 800 K) in systems with dust/gas ratios within a factor of ~10 of solar composition (i.e., $D/G$ ~0.1–10). Our equilibrium models for $T$ ~1000–1100 K for $P$ ~$10^{-6}$–$10^{-4}$ bar at $D/G = 1$ indicate olivine with MnO contents of ~0.8–0.9 wt.%, but with Fa and CaO contents significantly lower (~0.1 mol% and ~0.02–0.04 wt.%, respectively) than are observed for MnO-rich olivine (Table 4). Sugiura et al. (2009) suggested that diffusion of minor elements may have been too sluggish to allow equilibration of these elements in ~1–10 μm-diameter olivine grains in AOAs at temperatures below ~1100–1300 K. If so, condensation at $D/G \sim 1$ cannot produce MnO-rich olivine. However, this conclusion is tempered by the possibility of disequilibrium and somewhat uncertain diffusion rates for olivine.

Disequilibrium is suggested also for the forsteritic olivine grains in our study (Table 4), which are the least likely to have been affected by secondary processes. Although these forsterites have Mn and Ca contents similar to those predicted by equilibrium models at $T \sim 1130$–$1260$ K, $P \sim 10^{-6}$–$10^{-4}$ bar, and $D/G \sim 1$, the predicted Fa and especially $Cr_2O_3$ contents (~0.1 mol% and ~0.5–0.7 wt.%, respectively) are different than observed (~0.6 mol% and ~0.1 wt.%).

### 4.6. AOAs as precursors to chondrules?

In this section we show that the dominant olivine-rich lithology of AOAs could have been a suitable precursor to olivine in Type I chondrules, based on trace element data for olivine. However, chondrules did not simply form by the melting of AOAs; open system exchange of oxygen and often silicon would have had to occur during melting.

We compared narrow-beam SIMS data for AOA olivine to a similar dataset for olivine in chondrules from Type 3 ordinary chondrites (Ruzicka et al., 2008b) to evaluate whether the main olivine-rich component of AOAs could have been a chemically suitable precursor for chondules. Olivine data for chondrules in ordinary chondrites were used as no comparable data exist for chondrules in carbonaceous chondrites.

The trace element composition of olivine in AOAs somewhat resembles that of olivine in chondrules but shows some important differences. For example, Fig. 12 shows Sc–Fe, Sc–Zr, Sc–Ti and Sc–Y variation diagrams for

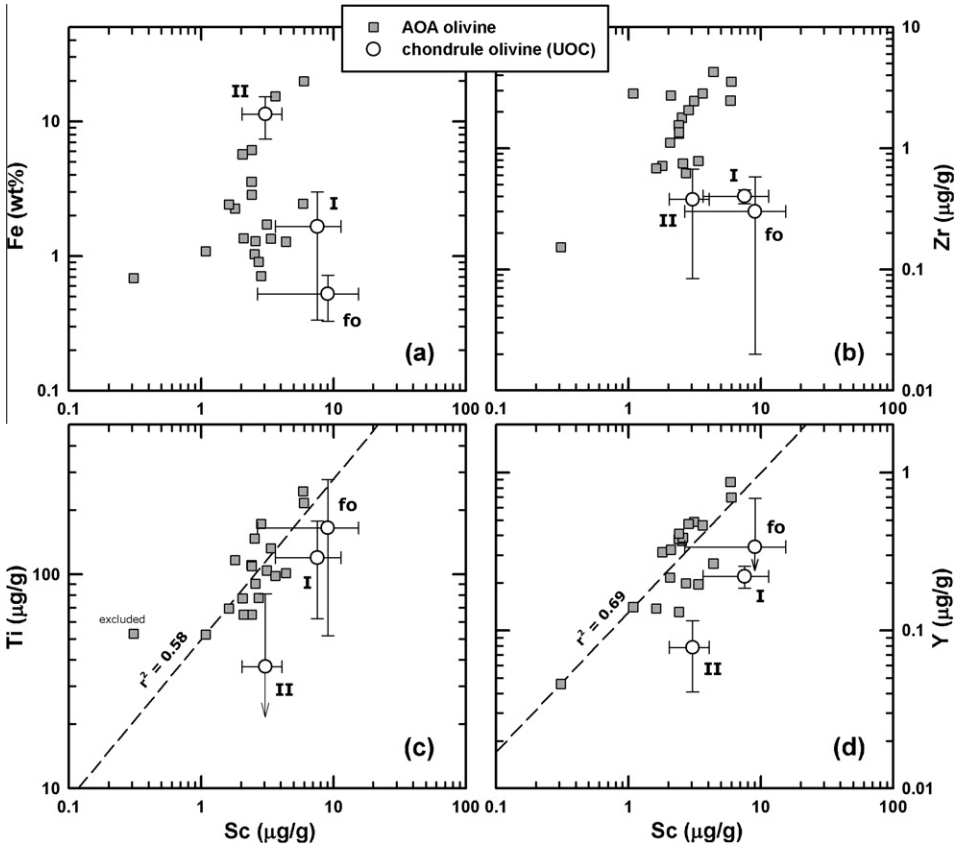


Fig. 12. Variation diagrams compare the composition of olivine in AOAs to that in chondrules from unequilibrated ordinary chondrites. Chondrule data are from Ruzicka et al. (2008b) and show mean compositions (points) and standard deviations (bars) for normal (non-relict) olivine in chondrules including forsterite (fo), grain cores in Type I chondrules, and grain cores in Type II chondrules. (a) Sc vs. Fe. (b) Sc vs. Zr. (c) Sc vs. Ti. (d) Sc vs. Y.

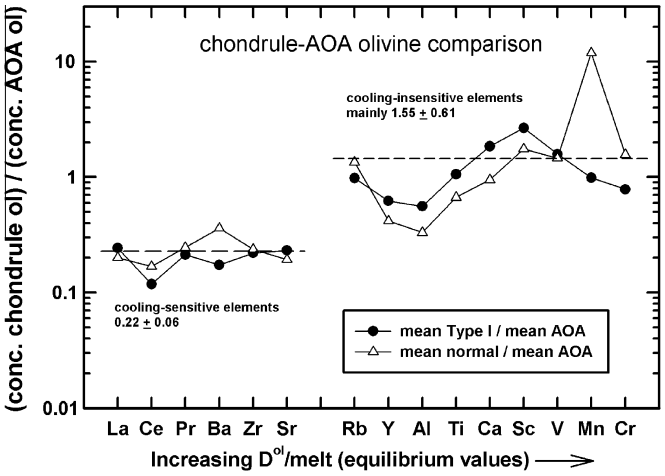


Fig. 13. Plot showing the average concentration ratio (chondrule olivine)/(AOA olivine) for lithophile trace and minor elements ordered according to mineral/melt partition coefficients in olivine (Ruzicka et al., 2008b). Highly incompatible (or cooling-sensitive) elements tend to depleted in chondrule olivine compared to AOA olivine (abundance in chondrule olivine ~0.2 × abundance in AOA olivine), whereas semi-incompatible (or cooling-insensitive) elements tend to have similar concentrations in the two types of objects, especially for Type I chondrules (Mn is strongly enriched in Type II chondrule olivine). Dashed lines indicate averages, excluding Mn for mean normal/mean AOA.

olivine. Olivine grains from AOAs have Fe contents most similar to that of Type I chondrules, but Sc contents tend to be lower and Zr contents higher in AOA olivine compared to chondrule olivine (Fig. 12a–b). In addition, although Sc concentrations are correlated with Ti and Y for both chondrule and AOA olivine, data arrays are offset to higher Sc values for chondrules (Fig. 12c–d). Thus, it is clear that chondrule olivine cannot have been derived from AOA olivine without chemical modification.

More generally, the chemical differences between AOA and chondrule olivine for any given element appears to be somewhat related to the compatibility of the element ($D$ = olivine/melt partition coefficient). This is illustrated in Fig. 13, which shows average (chondrule olivine)/(AOA olivine) concentration ratios for lithophile elements according to $D$-values. This comparison is made for both Type I chondrule olivine and for all normal (non-relict Type I and Type II) chondrule olivine, but similar results are obtained for both. Namely, compared to AOA olivine, chondrule olivine is consistently depleted in those elements that are highly incompatible (La, Ce, Pr, Ba, Sr, Zr), whereas (chondrule olivine)/(AOA olivine) concentration values are similar or high for elements that are less incompatible (Rb, Y, Al, Ti, Ca, Sc, V, Mn, Cr) (Fig. 13). Concentrations for the former elements in chondrule olivine are controlled by rapid cooling effects, whereas those for the latter more reflect the compositions of the melts from which the olivine crystallized (Ruzicka et al., 2008b). Manganese is strongly enriched in ferroan (Type II) chondrule olivine compared to AOA olivine, resulting in a high concentration ratio for this element in Fig. 13.

These olivine data are consistent with a simple model in which (1) AOA olivine was a major precursor component to chondrule olivine, and (2) elements were redistributed by igneous fractionation during chondrule formation. There is no obvious correlation involving element volatility, so vapor-fractionation effects were less important than igneous effects. During melting, the more highly incompatible elements would tend to redistribute from olivine into a melt fraction (but not as much as one might expect owing to disequilibrium caused by rapid cooling), lowering their abundance in newly-crystallized olivine. Similarly, the semi-incompatible elements would tend not to fractionate as much into melt, so their concentration in newly crystallizing olivine would not be decreased as much, if at all. The overall effect would be to result in lower olivine chondrule/AOA concentration ratios for highly incompatible elements than for semi-incompatible elements, as observed. The model is oversimplified in that it neglects the effects of other phases in the melting process involved to form chondrules. However, the fact that highly incompatible elements have concentration ratios $<1$ and semi-incompatible elements have concentration ratios $\geqslant 1$ implies that AOA olivine could have been a generally suitable precursor to chondrule olivine. Otherwise, the element ratios for the two sets of elements might be either both $<1$ or both $>1$.

This model can be used to explain variation diagrams such as Fig. 12. The net effect of melting and crystallization processes resulted in higher Sc contents in olivine, because it is a relatively compatible element whose original concentration in AOA olivine was less than the new equilibrium concentration imposed by mineral-melt partitioning. In contrast, Zr is much more incompatible, so it partitioned strongly into melt, resulting in lower Zr contents and much lower Zr/Sc values in chondrule olivine than in AOA olivine (Fig. 12b). Titanium and Y concentrations for olivine did not undergo much net change during melting, because these elements are neither highly incompatible nor as compatible as Sc. Although Ti and Y contents could have changed somewhat, the main effect was a shift to higher Sc contents (Fig. 12c–d). Iron partitioning would depend on redox conditions during chondrule formation (the same is true for V and Cr), as well as on the amount of FeO enrichment caused by secondary modification prior to melting

(Section 4.5). Nonetheless, the generally similar Fe contents in most AOA olivine and Type I chondrules (Fig. 12a) suggests that AOA olivine could have been a precursor to Type I chondrules. Thus, we infer that the combined effects of melting and crystallization during chondrule formation resulted in olivine with higher Sc, lower Zr, and similar Fe, Ti, and Y contents compared to the precursor material.

Chondrules did not form simply by the melting of AOAs in a closed system. Given the $^{16}$O-rich composition of AOAs compared to chondrules (e.g., Yurimoto et al., 2008), we suggest that ferromagnesian chondrules were formed by melting in a gaseous reservoir that was less $^{16}$O-rich than that which produced AOAs, and that open-system exchange of oxygen between melt and gas occurred. A shift in nebular gas composition to less $^{16}$O-rich values has been inferred by many workers (e.g., Wasson et al., 2004; Kunihiro et al., 2004; Ruzicka et al., 2007; Yurimoto et al., 2008). Diffusion of oxygen is fairly rapid in melt, but slow in minerals such as olivine, suggesting that changes in oxygen-isotope composition during chondrule formation would require exchange to occur while the objects were molten (Ruzicka et al., 2007). Multiple episodes of melting and gas–solid exchange could conceivably explain the variations in oxygen-isotopic compositions that are observed for different grains in chondrules (e.g., Ruzicka et al., 2007).

Most AOAs have bulk compositions that lie on the Si-poor (larnite-rich) side of the forsterite-anorthite join (thermal divide) in the forsterite-larnite-corundum ternary (Fig. 9). In general, AOAs are too Si-poor to be suitable as chondrule precursors (McSween, 1977; Komatsu et al., 2001; Krot et al., 2004b,c, 2006). Thus, melting of AOAs to form chondrules would appear to require an open-system influx of Si (Krot et al., 2004b,c, 2005). An influx of Si into molten chondrules has been proposed based on the properties of chondrules and experiments (Hewins et al., 2005; Libourel et al., 2006), making this process of AOA transformation plausible.

Some AOAs in our dataset lie on the larnite-poor side of the forsterite-anorthite divide and in this way resemble the bulk compositions of ferromagnesian chondrules (Fig. 9). Among these are objects that contain elevated amounts of low-Ca pyroxene, including Ef-12 (Fig. 1g), Leo-10 (Fig. 1i), and Ef-18 (Fig. 1j). These objects could have been melted to produce chondrules without necessarily requiring additional Si enrichment. Moreover, two of these objects (Leo-10 and Ef-18) have poikilitic-textured peripheries that resemble the textures of some chondrules, suggesting that they were melted on their peripheries.

Altogether, our data support the idea that AOAs may have formed at an intermediate stage in the evolution of nebular solids, between CAIs on the one hand and Type I chondrules on the other. Features linking AOAs to CAIs include the presence of CAI-like nodules and ribbons within AOAs, the similar mineralogy of Ca-Al-rich phases, the similar oxygen isotope compositions of AOAs and CAIs, and the moderately refractory bulk compositions for most AOAs. Features linking AOAs to chondrules include the composition of olivine and the presence of some objects with Si-enriched compositions and igneous textures.

## 5. CONCLUSION

Petrographic and microchemical data for amoeboid olivine aggregates (AOAs) in three reduced CV chondrites (Efremovka, Leoville, and Vigarano) support the idea that AOAs formed by dust growth as condensates in the solar nebula. The objects appear to serve as a bridge between CAIs and chondrules. Specifically:

(1) Fractional condensation or fractional vaporization was important in forming various AOA assemblages, including the chief olivine component, as well as spinel + Ca-pyroxene and Ca-pyroxene + anorthite assemblages that have Group II trace element patterns
(2) Ca-pyroxene + anorthite assemblages within AOAs appear to have formed by reaction of CAIs with Mg-Si-rich gas.
(3) Different refractory assemblages in some individual AOAs formed under different nebular conditions and were not equilibrated following agglomeration.
(4) Vaporization appears to have been important in producing some spinel-rich materials.
(5) Bulk AOAs formed by the mixing of condensates produced at different temperatures. Formation at a pressure of $\sim10^{-6}$–$10^{-4}$ bar and temperature of $\sim$1200–1384 K in a system of canonical solar composition satisfies most of the chemical and petrographic constraints for AOAs, but temperatures and pressures may have been higher for the most refractory, spinel-rich materials.
(6) An apparent paucity of metal in most AOAs compared to the predictions of equilibrium condensation models can be explained by differential aerodynamic sorting between olivine and metal caused by differences in mineral density.
(7) The composition of olivine in Efremovka, Leoville, and Vigarano AOAs reflects disequilibrium and secondary processes. MnO-rich olivine in Efremovka may have formed by low-temperature processes (cryptic aqueous alteration, or disequilibrium condensation).
(8) Some AOA-like objects show chemical and textural similarities to chondrules. Trace element data for olivine are consistent with a simple model in which AOA olivine was a precursor to Type I chondrule olivine, with elements redistributed by igneous fractionation during melting. Chondrules could have been derived from AOA-like precursors following gas–melt chemical and isotopic exchange in an environment different than that which AOAs originally formed.

## ACKNOWLEDGMENTS

This work was supported by NASA Grant NNG06GE17G (A.R.). We thank Mike Weisberg, Misha Petaev, and Naoji Sugiura for helpful reviews that improved the quality of this manuscript, and Sasha Krot for editorial handling.

## APPENDIX A. DETAILS ON EXPERIMENTAL CONDITIONS AND METHODS

### A.1. Electron microprobe

Major and minor elements were analyzed using an electron microprobe at Oregon State University in wavelength-dispersive mode. Operating conditions included a 15 keV accelerating voltage and a beam current of 50 nA. Well-characterized minerals and glasses were used as standards, and data were reduced using the nominal Cameca PAP procedure (Pouchou and Pichoir, 1985).

Nominal criteria for accepting analyses as olivine included 3.975–4.025 cations/4 oxygen; 1.9–2.1 M/Si, where M = the sum of cations other than Si; and analysis totals between 97–102 wt.%. Despite these criteria, analyses of olivine sometimes showed elevated Al or Ca contents possibly reflecting beam overlap effects with other phases (Kornacki and Wood, 1984), so all EMPA analyses of this phase were further evaluated by creating plots that showed how measured concentrations compared to hypothetical mixing trends for various minerals. On this basis, analyses of olivine showing both elevated CaO (>0.3 wt.%) and $Al_2O_3$ (>0.9 wt.%) were excluded as likely reflecting contamination by Ca-rich pyroxene, and analyses showing high $Al_2O_3$ alone (>1 wt.%) were excluded as likely reflecting contamination by anorthite or spinel.

### A.2. Norm calculation

"Defocused" beam EMPA data (DB-EMPA) were obtained to estimate mineral proportions in analysis areas using a norm calculation. The calculation assumes as possible normative minerals the phases that are found in AOAs. These include: olivine, Ca-rich pyroxene (the sum of normative diopside, hedenbergite, Ca-Tschermak), anorthite, low-Ca pyroxene (enstatite + ferrosilite), metal (with assumed 7 wt.% Ni – Weisberg et al., 2004), spinel ($MgAl_2O_4$ spinel + hercynite + chromite + picrochromite), melilite (gehlenite + akermanite), nepheline, and sodalite. All S was assumed to be associated with troilite, but sulfide is rare in AOAs and the actual siting of S was not determined. All Fe remaining after assignment to troilite and metal was partitioned in olivine and pyroxene according to apparent Mg#. The following mineral densities ($\rho$, all in g/cm$^3$ and based on Gaines et al., 1997) were assumed to convert weight to volume fractions for mineral phases: $\rho_{forsterite} = 3.22$, $\rho_{fayalite} = 4.39$, $\rho_{diopside} = 3.28$, $\rho_{hedenbergite} = 3.65$, $\rho_{Ca\text{-}Tschermak} = 3.28$, $\rho_{enstatite} = 3.20$, $\rho_{ferrosilite} = 4.00$, $\rho_{anorthite} = 2.76$, $\rho_{metal} = 7.97$, $\rho_{spinel} = 3.58$, $\rho_{hercynite} = 4.26$, $\rho_{chromite} = 5.06$, $\rho_{picrochromite} = 4.41$, $\rho_{sodalite} = 2.3$, $\rho_{nepheline} = 2.63$, $\rho_{troilite} = 4.84$, $\rho_{gehlenite} = 3.05$, $\rho_{akermanite} = 3.94$. Based on the ability to account for the chemical and petrographic data, the norm calculation appears to be relatively robust for the olivine-rich assemblages typically found in AOAs. It appears to be less accurate for CAI-like assemblages.

### A.3. Ion microprobe

SIMS was used to analyze trace elements at Washington University according to the techniques of Zinner and Crozaz (1986a). Analyses were made using an $O^-$ primary beam and energy filtering at low mass resolution to remove complex molecular interferences. The resulting mass spectrum was deconvolved in the mass ranges K–Ca–Sc–Ti and Rb–Sr–Y–Zr to remove simple molecular interferences that are not eliminated with energy filtering (Alexander, 1994; Hsu, 1995). Sensitivity factors for the REE in plagioclase are from Floss and Jolliff (1998); those for pyroxene are from Zinner and Crozaz (1986b). Sensitivity factors for other elements based on various silicate standards are from Hsu (1995) and are listed in Table 1 of Floss et al. (1998). For mixed phases, average sensitivity factors are used for Mg, Fe and Ca, and average non-plagioclase sensitivity factors are assumed for the REE. Absolute concentrations were determined by normalizing ion signal concentrations to concentrations determined by electron microprobe analysis, nominally using Si as the normalizing element.

Each SIMS analysis was evaluated to take into account the possibility of analyzing off the desired target area. Apparent concentrations derived by SIMS were compared to concentrations obtained by EMPA for the same elements at the same or nearby location. For both narrow beam and broad beam analyses, if SIMS and EMPA values agreed substantially, the analysis was accepted as is. If the values did not substantially agree for narrow beam SIMS, the analysis was rejected. If the values did not substantially agree for broad beam SIMS, the SIMS data were instead renormalized to the sum of elements as determined by EMPA. In practice, this renormalization resulted in less extreme, reasonable compositions. Two-step normalizations were most commonly used for spinel-rich regions.

For broad beam "on target" analyses ($N = 49$), average SIMS/EMPA concentration ratios based on Si normalizations average close to 1 for Mg (0.99), Ca (1.03), Cr (1.04), Mn (1.12), Al (1.14), and for analysis totals (1.02), and have somewhat higher values for Na (1.92), Fe (1.48), and Ni (2.07). The many values close to 1 indicate generally good agreement between the two techniques and suggest that bulk compositions derived by the two techniques are generally valid. Higher values for Na are attributed to relatively poor EMPA determinations caused by this element having concentrations close to background values for EMPA, and higher values for Fe and Ni are explained by slight oversampling of metal in some of the SIMS analyses.

### A.4. Thermodynamic modeling

For comparison to AOA data, we used a version of the CWPI thermodynamic code (Petaev and Wood, 1998, 2005), developed and kindly provided by Mikhail Petaev, to model condensate compositions in a 20-element system (H, He, C, N, O, Na, Mg, Al, Si, P, S, Cl, K, Ca, Ti, Cr, Mn, Fe, Co, Ni). For all runs, isobaric conditions and complete equilibrium (no isolation of condensates) were

assumed so as to minimize the number of free parameters. Investigated system compositions included "cosmic", based on the average composition of CI chondrites (Anders and Grevesse, 1989), and "dust-enriched" systems (e.g., Wood and Hashimoto, 1993; Ebel and Grossman, 2000).

## REFERENCES


Aléon J., Krot A. N. and McKeegan K. D. (2002) Ca–Al-rich inclusions and amoeboid olivine aggregates from the CR carbonaceous chondrites. *Meteorit. Planet. Sci.* **37**, 1729–1755.

Alexander C. M. O'D. (1994) Trace element distributions within ordinary chondrite chondrules: implications for chondrule formation conditions and precursors. *Geochim. Cosmochim. Acta* **58**, 3451–3467.

Anders E. and Grevesse N. (1989) Abundances of the elements: meteoritic and solar. *Geochim. Cosmochim. Acta* **53**(1989), 197–214.

Bonal L., Quirico E., Bourot-Denise M. and Montagnac G. (2006) Determination of the petrologic type of CV3 chondrites by Raman spectroscopy of included organic matter. *Geochim. Cosmochim. Acta* **70**, 1849–1863.

Boynton W. V. (1975) Fractionation in the solar nebula: condensation of ytrrium and the rare earth elements. *Geochim. Cosmochim. Acta* **39**, 569–584.

Boynton W. V. (1978) Rare-earth elements as indicators of supernova condensation. *Lunar Planet. Sci. IX*, 120–1122.

Boynton W. V. (1985) Meteoritic evidence concerning conditions in the solar nebula. In *Protostars and Planets* (eds. D. C. Black and M. S. Matthews). University of Arizona Press, Tucson, pp. 772–787.

Boynton W. V. and Cunningham C. C. (1981) Condensation of refractory lithophile trace elements in the solar nebula and in supernovae. *Lunar Planet Sci. XII*, 106–108.

Chizmadia L. J., Rubin A. E. and Wasson J. T. (2002) Mineralogy and petrology of amoeboid olivine inclusions in CO3 chondrites: relationship to parent-body aqueous alteration. *Meteorit. Planet. Sci.* **37**, 1781–1796.

Cuzzi J. and Weidenschilling S. J. (2006) Particle-gas dynamics and primary accretion. In *Meteorites and the Early Solar System II* (eds. D. S. Lauretta and Jr. H. Y. McSween). University of Arizona Press, Tucson, pp. 353–381.

Davis A. M. and Grossman L. (1979) Condensation and fractionation of rare earths in the solar nebula. *Geochim. Cosmochim. Acta* **43**, 1611–1632.

Davis A. M., Tanaka T., Grossman L., Lee T. and Wasserburg G. J. (1982) Chemical composition of HAL, an isotopically unusual Allende inclusion. *Geochim. Cosmochim. Acta* **46**, 1627–1651.

Ebel D. S. and Grossman L. (2000) Condensation in dust-enriched systems. *Geochim. Cosmochim. Acta* **64**, 339–366.

Ebel D. S. and Weisberg M. K. (2011) Thermodynamic stability of low-iron manganese-enriched olivine in the solar nebula. *Meteorit. Planet. Sci.* **46**. Abstract #5500.

Fagan T. J., Krot A. N., Keil K. and Yurimoto H. (2004) Oxygen isotopic evolution of amoeboid olivine aggregates in the reduced CV3 chondrites Efremovka, Leoville, and Leoville. *Geochim. Cosmochim. Acta* **68**, 2591–2611.

Floss C. and Jolliff B. (1998) Rare earth element sensitivity factors in calcic plagioclase (anorthite). In *Secondary Ion Mass Spectrometry, SIMS XI* (eds. G. Gillen, R. Lareau, J. Bennett and F. Stevie). John Wiley & Sons, Chichester, England, pp. 785–788.

Floss C., James O. B., McGee J. J. and Crozaz G. (1998) Lunar ferroan anorthosite petrogenesis: clues from trace element distributions in FAN subgroups. *Geochim. Cosmochim. Acta* **62**, 1255–1283.

Gaines R. V., Skinner H. C. W., Foord E. E., Mason B. and Rosenzweig A. (1997) *Dana's New Mineralogy—The System of Mineralogy of James Dwight Dana and Edward Salisbury Dana*, 8th ed. John Wiley & Sons Inc, New York, 1819 pp.

Grossman L. (1974) Amoeba-shaped olivine aggregates: a new type of inclusion in the Allende meteorite. *Meteoritics* **9**, 348–349.

Grossman L. and Steele I. M. (1976) Amoeboid olivine aggregates in the Allende meteorite. *Geochim. Cosmochim. Acta* **40**, 149–155.

Grossman L., Ganapathy R., Methot R. L. and Davis A. M. (1979) Trace elements in the Allende meteorite amoeboid olivine aggregates. *Geochim. Cosmochim. Acta* **43**, 817–829.

Hewins R. H., Connolly H. C., Lofgren G. E. and Libourel G. (2005) Experimental constraints on chondrule formation. In *Chondrites, the Protoplanetary Disk* (eds. A. N. Krot, E. R. D. Scott and B. Reipurth). Astronomical Society of the Pacific, San Francisco, pp. 286–316.

Hiyagon H. and Hashimoto A. (1999) $^{16}O$ excesses in olivine inclusions in Yamato-86009 and Murchison chondrites and their relation to CAIs. *Science* **283**, 828–831.

Hsu W. (1995) Ion microprobe studies of the petrogenesis of enstatite chondrites and eucrites. Ph. D. Thesis, Washington University.

Huss G. R., MacPherson G. J., Wasserburg G. J., Russell S. S. and Srinivasan G. (2001) Aluminum-26 in calcium-aluminum-rich inclusions and chondrules from unequilibrated ordinary chondrites. *Meteorit. Planet. Sci.* **36**, 975–997.

Hutchison R. (2004) *Meteorites—A petrologic, chemical and isotopic synthesis.* Cambridge University Press. pp. 506.

Jarosewich E. (1990) Chemical analyses of meteorites: a compilation of stony and iron meteorite analyses. *Meteoritics* **25**, 323–337.

Kerridge J. F. (1979) Fractionation of refractory lithophile elements among chondritic meteorites. *Proc. Lunar Planet. Sci. Conf.* **10**, 989–996.

Klöck W., Thomas K. L., McKay D. S. and Palme H. (1989) Unusual olivine and pyroxene composition in interplanetary dust and unequilibrated ordinary chondrites. *Nature* **339**, 126–128.

Komatsu M., Krot A. N., Petaev M. I., Ulyanov A. A., Keil K. and Miyamoto M. (2001) Mineralogy and petrography of amoeboid olivine aggregates from the reduced CV3 chondrites Efremovka, Leoville and Vigarano: products of nebular condensation, accretion and annealing. *Meteorit. Planet. Sci.* **36**, 629–641.

Kornacki A. S. and Wood J. A. (1984) The mineral chemistry and origin of inclusion matrix and meteorite matrix in the Allende CV3 chondrite. *Geochim. Cosmochim. Acta* **48**, 1663–1676.

Krot A. N., Meibom A. and Keil K. (2000a) A clast of Bali-like oxidized material in the reduced CV chondrite breccia Vigarano. *Meteorit. Planet. Sci.* **35**, 817–825.

Krot A. N., Brearley A. J., Petaev M. I., Kallemeyn G. W., Sears D. W. G., Benoit P. H., Hutcheon I. D., Zolensky M. E. and Keil K. (2000b) Evidence for low-temperature growth of fayalite and hedenbergite in MacAlpine Hills 88107, an ungrouped carbonaceous chondrite related to the CM-CO clan. *Meteorit. Planet. Sci.* **35**, 1365–1386.

Krot A. N., Scott E. R. D., McKeegan K. D., Leshin L. A. and MacPherson G. J. (2002) Existence of an $^{16}O$-rich gaseous reservoir in the solar nebula. *Science* **295**, 1051–1054.

Krot A. N., Petaev M. I., Russell S. S., Itoh S., Fagan T. J., Yurimoto H., Chizmadia L., Weisberg M. K., Komatsu M., Ulyanov A. A. and Keil K. (2004a) Amoeboid olivine aggregates and related objects in carbonaceous chondrites: records of nebular and asteroidal processes. *Chem. Erde* **64**, 185–239.

Krot A. N., Petaev M. I. and Yurimoto H. (2004b) Amoeboid olivine aggregates with low-Ca pyroxenes: a genetic link between refractory inclusions and chondrules? *Geochim. Cosmochim. Acta* **68**, 1923–1941.

Krot A. N., Fagan T. J., Keil K., McKeegan K. D., Sahijpal S., Hutcheon I. D., Petaev M. I. and Yurimoto H. (2004c) Ca, Al-rich inclusions, amoeboid olivine aggregates, and Al-rich chondrules from the unique carbonaceous chondrite Acfer 094: I. Mineralogy and petrology. *Geochim. Cosmochim. Acta* **68**, 2167–2184.

Krot A. N., Petaev M. I. and Bland P. A. (2004d) Multiple formation mechanisms of ferrous olivine in CV carbonaceous chondrites during fluid-assisted metamorphism. *Antarct. Meteorite Res.* **17**, 153–171.

Krot A. N., Fagan T. J., Nagashima K., Petaev M. I. and Yurimoto H. (2005) Origin of low-Ca pyroxene in amoeboid olivine aggregates: evidence from oxygen isotopic compositions. *Geochim. Cosmochim. Acta* **69**, 1873–1881.

Krot A. N., Petaev M. I. and Keil K. (2006) Mineralogy and petrology of Al-rich objects and amoeboid olivine aggregates in the CH carbonaceous chondrite North West Africa 739. *Chem. Erde* **66**, 57–76.

Kunihiro T., Rubin A. E., McKeegan K. D. and Wasson J. T. (2004) Oxygen isotope compositions of relict and host grains in chondrules and the Yamato 81020 CO3.0 chondrite. *Geochim. Cosmochim. Acta* **68**, 3599–3606.

Larimer J. W. (1979) The condensation and fractionation of refractory lithophile elements. *Icarus* **40**, 446–454.

Larimer J. W. and Anders E. (1970) Chemical fractionations in meteorites—III. Major element fractionations in chondrites. *Geochim. Cosmochim. Acta* **34**, 367–387.

Larimer J. W. and Wasson J. T. (1988) Refractory lithophile elements. In *Meteorites and the Early Solar System* (eds. J. F. Kerridge and M. S. Mathhews). University of Arizona Press, Tucson, pp. 394–415.

Libourel G., Krot A. M. and Tissandier L. (2006) Role of gas-melt interaction during chondrule formation. *Earth Planet. Sci. Lett.* **251**, 232–240.

Lodders K. (2003) Solar system abundances and condensation temperatures of the elements. *Astrophys. J.* **591**, 1220–1247.

Ma C. and Rossman G. R. (2009) Grossmanite, $CaTi^{3+}AlSiO_6$, a new pyroxene from the Allende meteorite. *Am. Mineral.* **94**, 1491–1494.

Ma C., Beckett J. R. and Rossman G. R. (2010) Grossmanite, davisite, and kushiroite: three newly approved diopside-group clinopyroxenes uin CAIs. *Lunar Planet. Sci. 41st*. #1494 (abstr.).

Mason B. and Taylor S. R. (1982) Inclusions in the Allende meteorite. *Smithson Contrib. Earth Sci.* **19**, 84–95.

McSween, Jr., H. Y. (1977) Chemical and petrographic constraints on the origin of chondrules and inclusions in carbonaceous chondrites. *Geochim. Cosmochim. Acta* **41**, 1843–1860.

Nakamura T., Noguchi T., Tschuiyama A., Ushikubo Kita. N. T., Valley J. W., Zolensky M. E., Kakazu Y., Sakamoto K., Mashio K. and Nakano T. (2008) Chondrulelike objects in short-period comet 81P/Wild 2. *Science* **321**, 1664–1667.

Petaev M. I. and Wood J. A. (1998) The condensation and partial isolation (CWPI) model of condensation in the solar nebula. *Meteorit. Planet. Sci.* **33**, 1123–1137.

Petaev M. I. and Wood J. A. (2005) Meteoritic constraints on temperatures, pressures, cooling rates, chemical compositions, and modes of condensation in the solar nebula. In *Chondrites and the Protoplanetary Disk*, vol. 341 (eds. A. N. Krot, E. R. D. Scott and B. Reipurth). ASP Conference Series, pp. 373–406.

Pouchou J. L. and Pichoir F. (1985) "PAP" procedure for improved quantitative microanalysis. In *Microbeam Analysis* (ed. J. T. Armstrong). San Francisco Press, Inc., San Francisco, pp. 104–106.

Rubin A. E. (1998) Correlated petrologic and geochemical characteristics of CO3 chondrites. *Meteorit. Planet. Sci.* **33**, 385–391.

Russell S.S., Krot A.N., Jeffries T.E. and Ulyanov A.A. (2003) Rare earth element systematics of fine-grained calcium-aluminum-rich inclusions and amoeboid olivine aggregates from Efremovka (CV3). *Lunar Planet. Sci. XXXIV*. #1631 (abstr.).

Russell S. S., Hartmann L., Cuzzi J., Krot A. N., Gounelle M. and Weidenschilling S. (2006) Timescales of the solar protoplanetary disk. In *Meteorites in the Early Solar System II* (eds. D. S. Lauretta and Jr. H. Y. McSween). University of Arizona Press, Tucson, pp. 233–251.

Ruzicka A. (1996) Petrologic-kinetic studies of meteorites. Ph. D. Dissertation, University of Arizona, pp. 300.

Ruzicka A., Hiyagon H., Hutson M. and Floss C. (2007) Relict olivine, chondrule recycling, and the evolution of nebular oxygen reservoirs. *Earth Planet. Sci. Lett.* **257**, 274–289.

Ruzicka A., Floss C. and Hutson M. (2008a) Amoeboid olivine aggregates (AOAs) in the Efremovka ($CV_R$) chondrite: first SIMS trace-element results. *Lunar Planet Sci. XXXIX*, Lunar and Planetary Institute. #1764 (abstr.).

Ruzicka A., Floss C. and Hutson M. (2008b) Relict olivine grains, chondrule recycling, and implications for the chemical, thermal, and mechanical processing of nebular materials. *Geochim. Cosmochim. Acta* **72**, 5530–5557.

Ruzicka A., Hutson M. L. and Floss C. (2011) Amoeboid olivine aggregate condensates and the origin of the refractory element fractionation. 4*2nd Lunar Planet. Sci. Conf*. #1336 (abstr.).

Scott E. R. D. and Krot A. N. (2005) Chondrites and their components. In *Meteorites, Comets, and Planets* (ed. A. Davis). El Sevier, Amsterdam, pp. 143–200.

Sugiura N., Petaev M. I., Kimura M., Miyazaki A. and Hiyagon H. (2009) Nebular history of amoeboid olivine aggregates. *Meteorit. Planet. Sci.* **44**, 559–572.

Wark D. A. (1979) Birth of the presolar nebula: the sequence of condensation revealed in the Allende meteorite. *Astrophys. Space Sci.* **65**, 275–295.

Wasson J. T. and Kallemeyn G. W. (1988) Compositions of chondrites. *Philos. Trans. R. Soc. London A* **325**, 535–544.

Wasson J. T., Rubin A. E. and Yurimoto H. (2004) Evidence in CO3.0 chondrites for a drift in the O isotopic composition of the solar nebula. *Meteorit. Planet. Sci.* **39**, 1591–1598.

Weisberg M. K., Prinz M., Kennedy A. and Hutcheon I. D. (1991) Trace elements in refractory-rich inclusions in CR2 chondrites. *Meteoritics* **26**, 407–408.

Weisberg M. K., Prinz M., Clayton R. N. and Mayeda T. K. (1993) The CR (Renazzo-type) carbonaceous chondrite group and its implications. *Geochim. Cosmochim. Acta* **57**, 1567–1586.

Weisberg M. K., Connolly H. C. and Ebel D. S. (2004) Petrology and origin of amoeboid olivine aggregates in CR chondrites. *Meteorit. Planet. Sci.* **39**, 1741–1753.

Weisberg M. K., Kita N. T., Ushikubo T., Connolly H. C., Jr., Ebel D.S., Spicuzza M. J. and Valley J.W. (2007) Petrologic-isotopic study of amoeboid olivine aggregates in CR chondrites. *Lunar Planet Sci. XXXVIII*. #1588 (abstr.).

Weisberg M. K., Ebel D. S., Connolly, Jr., H. C., Kita N. T., Ushikubo T. and Valley J. W. (2008) Metal-rich olivine aggregates in the Renazzo CR chondrite. *Meteorit. Planet. Sci.* **43**. Abstract #5125.

Wood J. A. and Hashimoto A. (1993) Mineral equilibrium in fractionated nebular systems. *Geochim. Cosmochim. Acta* **57**, 2377–2388.

Yurimoto H., Krot A. N., Choi B.-G., Aléon J., Kunihiro T. and Brearley A. J. (2008) Oxygen isotopes of chondritic compo-

nents. In *Reviews in Mineralogy & Geochemistry*, vol. 68 (eds. G. J. MacPherson, D. W. Mittlefehldt, J. H. Jones and S. B. Simon). Mineralogical Society of America, Chantilly, pp. 141–186.

Zinner E. and Crozaz G. (1986a) A method for the quantitative measurement of rare earth elements by ion microprobe. *Intl. J. Mass Spectrom. Ion Processes* **69**, 17–38.

Zinner E. and Crozaz G. (1986b) Ion probe determination of the abundances of all the rare earth elements in single mineral grains. In *Secondary Ion Mass Spectrometry, SIMS V* (eds. A. Benninghoven, R. J. Colton, D. S. Simons and H. W. Werner). Springer-Verlag, New York, pp. 444–446.

Zolensky M. E. et al. (2006) Mineralogy and petrology of comet 81P/Wild 2 nucelus samples. *Science* **314**, 1735–1739.

Zolotov M. Y., Mironenko M. V. and Shock E. L. (2006) Thermodynamic constraints on fayalite formation on parent bodies of chondrites. *Meteorit. Planet. Sci.* **41**, 1775–1796.

*Associate editor:* Alexander N. Krot